Materials Science & Engineering A 902 (2024) 146634

Contents lists available at ScienceDirect

Materials Science & Engineering A

journal homepage: www.elsevier.com/locate/msea

Edge dislocation-induced high-temperature strengthening in the $Ti_{37}V_{15}Nb_{22}Hf_{23}W_3$ refractory high-entropy alloys

Wenjun Huang [a], Xuejiao Wang [a], Junwei Qiao [a,*], Xiaohui Shi [a], Peter K. Liaw [d], Yucheng Wu [b,c,**]

[a] Laboratory of High-Entropy Alloys, College of Materials Science and Engineering, Taiyuan University of Technology, Taiyuan, 030024, China
[b] Key Laboratory of Interface Science and Engineering of New Materials, Ministry of Education, Taiyuan University of Technology, Taiyuan, 030024, China
[c] National-Local Joint Engineering Research Center of Nonferrous Metals and Processing Technology, Hefei University of Technology, Hefei, 230009, China
[d] Department of Materials Science and Engineering, The University of Tennessee, Knoxville, TN, 37996-2200, USA

ARTICLE INFO

Keywords:
Refractory High-Entropy Alloy (RHEA)
Mechanical properties
High-temperature strength
Edge dislocation

ABSTRACT

The $Ti_{37}V_{15}Nb_{22}Hf_{23}W_3$ is a multi-principal refractory alloy with exceptional strength and ductility at room temperature. For potential high-temperature applications, it is of great significance to investigate the deformation mechanism at different temperatures through tensile tests. The yield strength (YS) has a substantial temperature dependency from 298 K to 473 K, nevertheless is insensitive between 473 K and 1073 K, with a large decline at 1223 K. At 1,073 K, the yield strength of 550 MPa is still maintained, which has nearly exceeded most commercial alloys. The transmission electron microscopy (TEM) experiments revealed that the plastic deformation was controlled by dislocation slip, and the degree of deformation was strongly related to the dislocation density. The proportion of edge dislocations gradually increases as the temperature rises. When the temperature reaches 1073 K, the deformed dislocations are almost all edge dislocations. Edge dislocations control the strength of the alloy at high temperatures. The yield strength of the alloy is predicted using the edge dislocation strengthening model, which is in good agreement with the experimental values. The excellent high-temperature mechanical properties of the $Ti_{37}V_{15}Nb_{22}Hf_{23}W_3$ RHEAs indicate that it is potential to be used in future.

1. Introduction

Structural materials with remarkable mechanical characteristics at higher temperatures are in considerable demand for the development of gas-turbine engines [1–3]. The demand for high-temperature materials continues to increase due to the potential for improved gas turbine efficiency by raising the operating temperature [4]. Because of their superior mechanical properties and great resistance to creep and fatigue at high temperatures, nickel-based superalloys are frequently utilized as the primary component in high-pressure turbines [4–6]. However, the operating temperatures of nickel-based superalloys are getting close to their melting points, which makes further improving turbine efficiency extremely difficult [1,7]. When the temperature, $T \geq 0.5T_m$, the nickel-based superalloys will undergo time-dependent plastic deformation under the continuous action of a constant load [2,8]. It is crucial to develop new high-temperature materials that can work at higher temperatures as a consequence.

Recently, the design of high-entropy alloys (HEAs) with a wide compositional range has evolved, opening up new directions for research into enhanced refractory structural materials [9–13]. The newly developed HEAs, which consist of four or more principal metallic elements in equiatomic or near-equiatomic ratios, exhibit remarkable strength and hardness [9,14], high resistance to oxidation [15,16], outstanding thermal stability, and resistance to softening at high temperatures [17–19]. Due to their outstanding mechanical properties at temperatures over 800 °C, and in some cases even up to 1500 °C, refractory HEAs (RHEAs) distinguish out among many types of HEAs [5, 20,21]. They outperform traditional Ni-based superalloys, such as NbMoTaW and VNbMoTaW RHEAs, which still have a yield strength of more than 400 MPa at 1600 °C [20].

The underlying physical origin of high-temperature strength in RHEAs is unknown. The conventional view is that the strength of a BCC

* Corresponding author.
** Corresponding author. Key Laboratory of Interface Science and Engineering of New Materials, Ministry of Education, Taiyuan University of Technology, Taiyuan, 030024, China.
E-mail addresses: qiaojunwei@gmail.com (J. Qiao), ycwu@hfut.edu.cn (Y. Wu).

https://doi.org/10.1016/j.msea.2024.146634
Received 18 January 2024; Received in revised form 17 April 2024; Accepted 12 May 2024
Available online 13 May 2024

alloy is controlled by screw dislocation [22]. For instance, a large number of long and straight dislocations are present in TiZrHfNbTa RHEAs, which is characteristic of screw dislocations [23,24]. However, at high temperatures (~773 K) the dislocation has considerable curvature and "viscous" motion, indicating a loss of a strong screw advantage [25]. In addition, it has recently been indicated that edge dislocations control the high-temperature strength of the RHEAs [26]. In NbTaTiV and CrMoNbV RHEAs, the percentage of dislocations measured as edge dislocations after deformation at 1173 K were 82 % and 64 %, respectively [26]. However, the evolution of dislocation types in the RHEAs with temperatures has been rarely reported.

In view of this, the $Ti_{37}V_{15}Nb_{22}Hf_{23}W_3$ RHEA developed by our group was chosen as our research object in this study. The $Ti_{37}V_{15}Nb_{22}Hf_{23}W_3$ RHEA, developed previously [27] using the natural mixing method, exhibits an excellent tensile yield strength (~980 MPa) and elongation (~20 %) combination, which is expected to break through the limitation shackles and application bottlenecks of RHEAs. The main objectives of the research in this study are as follows: first, to explore the potential of $Ti_{37}V_{15}Nb_{22}Hf_{23}W_3$ RHEA for high-temperature applications. We will study the mechanical properties of the alloy at room temperature (RT) up to 1227 K and investigate its micro-deformation mechanism at high temperatures. Secondly, we will examine the evolution of dislocation types in the alloy at various temperatures and explore the factors contributing to the absence of screw-type dislocations at high temperatures. Finally, the theory of edge-type dislocations' strength is established to predict the high-temperature strength of the alloy, and the reasons for the disparity between the theory and experimental values are discussed.

2. Experimental methods

The as-cast plates were fabricated by vacuum arc melting a combination of high-purity raw material elements (>99.9 atomic percent, at %) in a Ti-gettered argon environment. The atomic nominal composition of the plates was $Ti_{37}V_{15}Nb_{22}Hf_{23}W_3$. Each alloy ingot was turned and remelted more than 5–8 times to ensure chemical homogeneity before being drop-cast into water-cooled copper molds measuring 36 × 12 × 6 mm in size. For more detailed experimental steps, one could refer to Refs. [27,28].

Electro-discharge machining was used to create dog-bone-shaped specimens with a gauge length of 10 mm and a cross-sectional size of 3 × 1 mm for uniaxial tensile tests. The surfaces of the samples were polished with 180, 400, 800, 1,200, 1,500, up to 2000-grit SiC paper. Using a universal testing machine (Instron 5969), the tests were run at temperatures ranging from 298 K to 1227 K with a constant strain rate ($\dot{\varepsilon}$) of 0.001/s. The heating method used was infrared heating. Once it reached the desired testing temperature, it was maintained for 5 min. In order to prevent oxidation, the tested sample's surface was coated with a boron-nitride high-temperature resistant paint. To guarantee the veracity of the data, at least three samples were measured in each instance.

Transmission electron microscopy (TEM) and electron backscatter diffraction (EBSD) techniques were used to study the microstructures of the alloys under various experimental settings. The EBSD was conducted by Oxford C-swift with a Voltage of 20 kV, and the EBSD data were analyzed by the software of Channel-5 [29,30]. Before conducting the EBSD testing, argon ion polishing (IM4000plus) was performed with a voltage of 4 kV, an angle of 3°, and the time of ~2 h was used. The samples were mechanically reduced to a thickness of less than 50 μm before being punched into discs with a diameter of 3 mm for TEM investigations. Twinjet electropolishing was finally carried out at 20 V and - 25 °C using a solution consisting of 5 (vol%) perchloric acid, 35 vol% n-butanol, and 60 vol% methanol.

3. Results

Microstructural analysis for the as-cast $Ti_{37}V_{15}Nb_{22}Hf_{23}W_3$ RHEA is presented in Fig. 1. The EBSD-IPF and XRD images in Fig. 1(a) and (b), respectively, provide further insights that the as-cast alloy seems to be a single-phase body-centered-cubic (BCC) solid solution with a grain size of ~28.8 μm [Fig. 1(d)], which is the same as the previous results [27]. The corresponding grain-boundary map, which reflects high and low angles, is derived in Fig. 1(c) to qualitatively represent the extent of the misorientation between the adjacent grains [31]. A green solid line is used to indicate the low-angle grain boundary (LAGB), which is present among them and has a misorientation of 2°–15°. A high-angle grain boundary (HAGB), represented by a black solid line, is a grain boundary with a misorientation greater than 15°. The HAGBs are clearly visible, and there are more HAGBs, while there are fewer LAGBs, which is consistent with common as-cast samples [32].

The engineering stress-strain curves of as-cast $Ti_{37}V_{15}Nb_{22}Hf_{23}W_3$ BCC-RHEAs at different temperatures are shown in Fig. 2. Additionally, the influence of deformation temperature on the yield strength (σ_y), ultimate strength (σ_{ust}), and fracture elongation (ε_f) is also depicted. The σ_y of the $Ti_{37}V_{15}Nb_{22}Hf_{23}W_3$ alloy decreases significantly from 977 MPa at 298 K to 759 MPa at 473 K. After that, an approximate plateau is observed from 473 K to 873 K [Fig. 2(b)]. An increase in temperature to 1223 K significantly reduces the σ_y. Table 1 summarizes the σ_y, σ_{ust}, and ε_f of the $Ti_{37}V_{15}Nb_{22}Hf_{23}W_3$ RHEA at different temperatures. Individual data points represent the average of three independent tensile tests conducted under each condition. Standard deviations were determined from the three test results and are displayed as error bars in Fig. 2(b). The evolution trend of σ_{ust} with the temperature is similar to that of the σ_y. According to the basic theory for dislocation motion the critical stress (τ_{F-R}) required to activate the Frank-Read (F–R) dislocation source is described as follows [33,34]:

$$\tau_{F-R} = \alpha \frac{Gb}{L} \tag{1}$$

where L is the length of the dislocation source, G is the shear modulus, and b is the Burgers vector, and α is a constant. G is sensitive to the temperature and decreases with increasing the temperature [33,35]. Therefore, τ_{F-R} of the alloy decreases with increasing the temperature. That is to say, the movement of dislocations will become easier at high temperatures, that is, the strength of the alloy will decrease, as demonstrated in Fig. 2(b). The particular 'high-temperature plateau' found in the $Ti_{37}V_{15}Nb_{22}Hf_{23}W_3$ alloy, where the strength is found to be indepedent of the temperature at between 473 K and 873 K, is of special interest, with comparable results in other literatures [5,36–38]. While early studies suggested that cross-kinks in screw dislocations were potential contributors to high-temperature strength [36,39–41], more recent research suggests that it may be due to the presence of thermal super-jogging in edge dislocations, which act as strong obstacles to dislocation motion [1,26,36].

However, the fracture elongation of the $Ti_{37}V_{15}Nb_{22}Hf_{23}W_3$ alloy decreases sharply at 973–1073 K, almost drops to zero. This indicates that it undergoes a transition from the plastic to brittle fracture as the temperature increases, as shown in Fig. 2(b). The tensile fracture diagram in Fig. 3 also confirms the transtition of the alloy from ductile to brittle fracture under high-temperature tension. When the temperature is below 973 K, a significant number of dimples can be found on the fracture surface of the sample, which is considered as a typical morphology of ductile fracture [6,42]. As the temperature continues to rise, the dimples disappears, and only quasi-cleavage fractures appear [see Fig. 3(e-f)]. Generally, the mobility of metal atoms increases at high temperatures, which leads to a decrease in the barrier to dislocation movement [43,44]. Likewise, dislocation motion modes increase, such as cross-slip and climb [43,44]. Theoretically, dislocation movement becomes easier, and the fracture elongation of single-phase alloys increases with increasing the temperature [30,45]. But in fact, the $Ti_{37}V_{15}Nb_{22}Hf_{23}W_3$ alloy is brittle at high temperatures, as presented in Fig. 2(b) and 3(e-f). The specific reasons are analyzed in detail in the

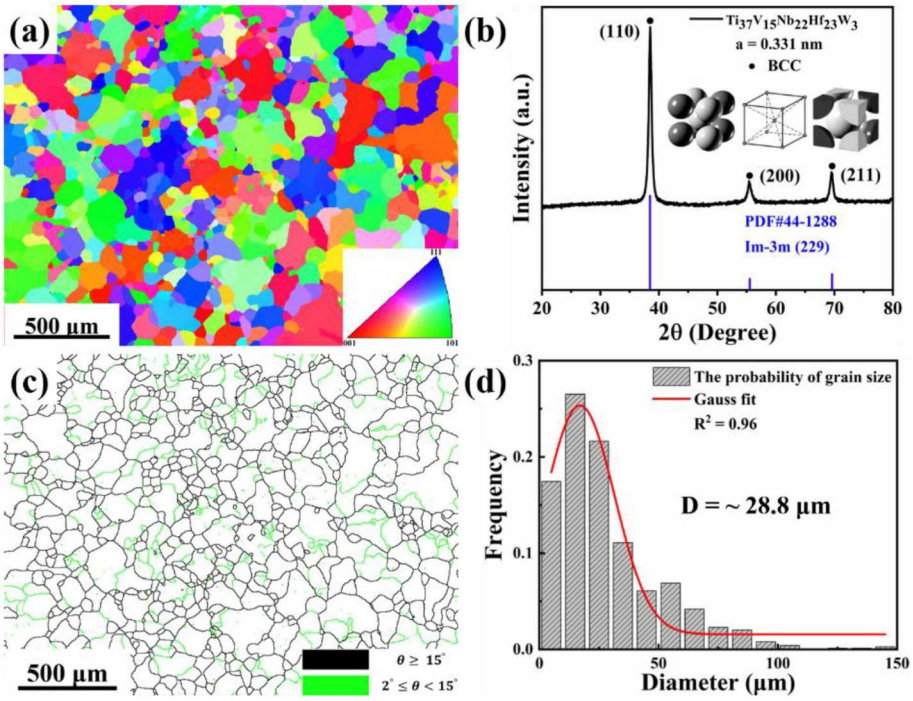

Fig. 1. Structural analysis of the as-cast $Ti_{37}V_{15}Nb_{22}Hf_{23}W_3$ RHEA. (a) EBSD inverse pole figure (IPF) map, (b) corresponding X-ray diffraction (XRD) pattern, (c) corresponding grain-boundary (GB) misorientaton mapping, and (d) corresponding grain-size distribution indicating an average size of 28.8 μm.

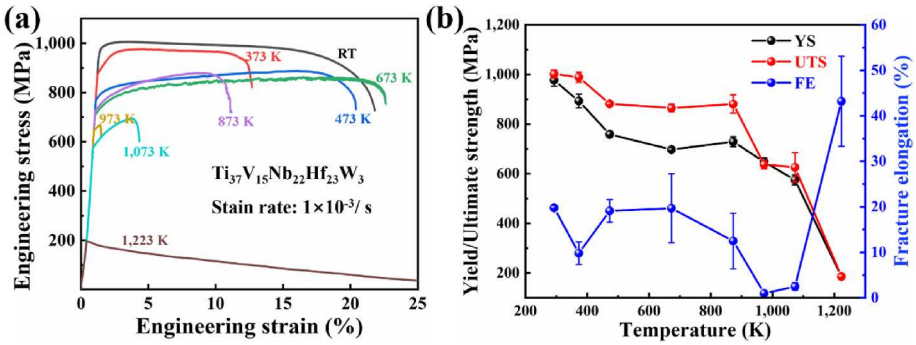

Fig. 2. (a) Tensile stress-strain curve of the as-cast $Ti_{37}V_{15}Nb_{22}Hf_{23}W_3$ RHEA at room temperature (RT) and high temperature (373–1223 K). (b) Temperature dependence of the yield strength (YS), the Ultimate strength (UTS) and the fracture elongation (FE) for the as-cast $Ti_{37}V_{15}Nb_{22}Hf_{23}W_3$ RHEA.

Table 1
Tensile mechanical properties of the $Ti_{37}V_{15}Nb_{22}Hf_{23}W_3$ RHEA at different temperature.

Temperature (K)	σ_y (MPa)	σ_{ust} (MPa)	ε_f (%)
293	977 ± 24	1002 ± 16	19.8 ± 0.6
373	893 ± 28	989 ± 20	9.8 ± 2.5
473	759 ± 13	882 ± 9	19.1 ± 2.5
673	697 ± 8	865 ± 16	19.7 ± 7.6
873	729 ± 20	881 ± 37	12.5 ± 6.1
973	648 ± 16	637 ± 17.3	1 ± 0
1073	575 ± 20	626 ± 59	2.5 ± 0.8
1223	186 ± 10	186 ± 10	43.2 ± 9.9

discussion section. When the temperature reaches 673 K, serrated flows are detected. These flows are believed to be caused by localized heterogeneous deformation, specificallly the interaction between dislocations and local stress field induced by the rough local atomic environment [1]. It is noticed that as the temperature exceeds 673 K, the serrated flows become less evident, indicating that a diffusion-mediated deformation process may become relevant.

The $Ti_{37}V_{15}Nb_{22}Hf_{23}W_3$ alloy has a higher yield strength than most typical superalloys. The temperature dependence of the yield strength of this alloy and other popular superalloys [1,5,17,21,27,46–48] as a function of testing temperature and homologous temperature, i.e., the ratio of testing temperature/melting temperature (T/T_m), is summarized in Fig. 4. The $Ti_{37}V_{15}Nb_{22}Hf_{23}W_3$ RHEA, which contains elements with high melting points (T_m), exhibits greater yield strengths at high temperatures [5,20]. For example, the yield strength of the studied alloy is approximately 300 MPa higher than that of Haynes 230 and about 100 MPa higher than that of Waspaloy (a nickel-based superalloy) in the temperature range of 298–1,073 K [Fig. 4(a)]. However, the high-temperature performance is comparable to that of the common TiZrHfNbTa RHEA [Fig. 4(a)]. If we switch to the specific strength perspective, the $Ti_{37}V_{15}Nb_{22}Hf_{23}W_3$ alloy shows incomparable and obvious advantages compared to the TiZrHfNbTa RHEA [Fig. 4(c)]. Like most metals and alloys [5,17,48], the strength of the metals and alloys decreases rapidly when the temperature exceeds 1,073 K [Fig. 4(a)]. This is because the activation of the diffusion-controlled deformation mechanism occurs above ~0.5–0.6 T_m, thereby leading to the softening of materials [Fig. 4(b)] [1,49,50]. The high-temperature performance of

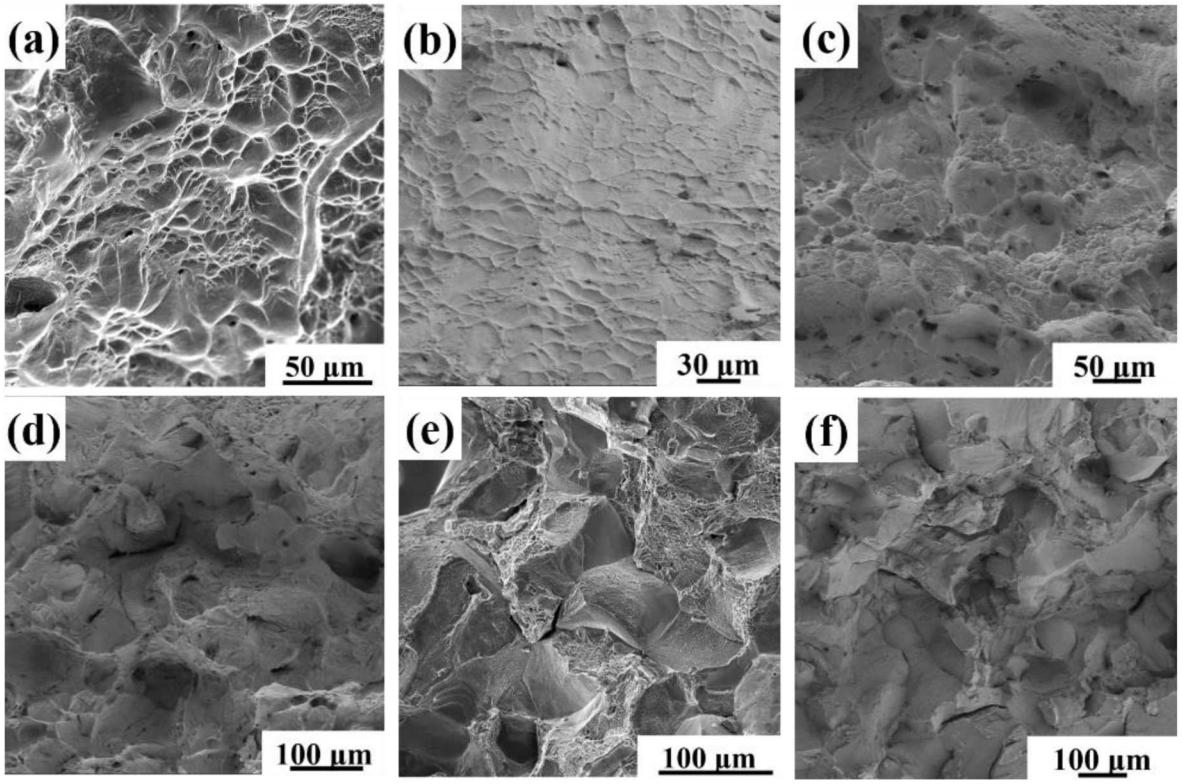

Fig. 3. The fracture morphology of the as-cast $Ti_{37}V_{15}Nb_{22}Hf_{23}W_3$ RHEA at different temperatures: (a) 373 K, (b) 473 K, (c) 673 K, (d) 873 K, (e) 973 K, and (f) 1073 K.

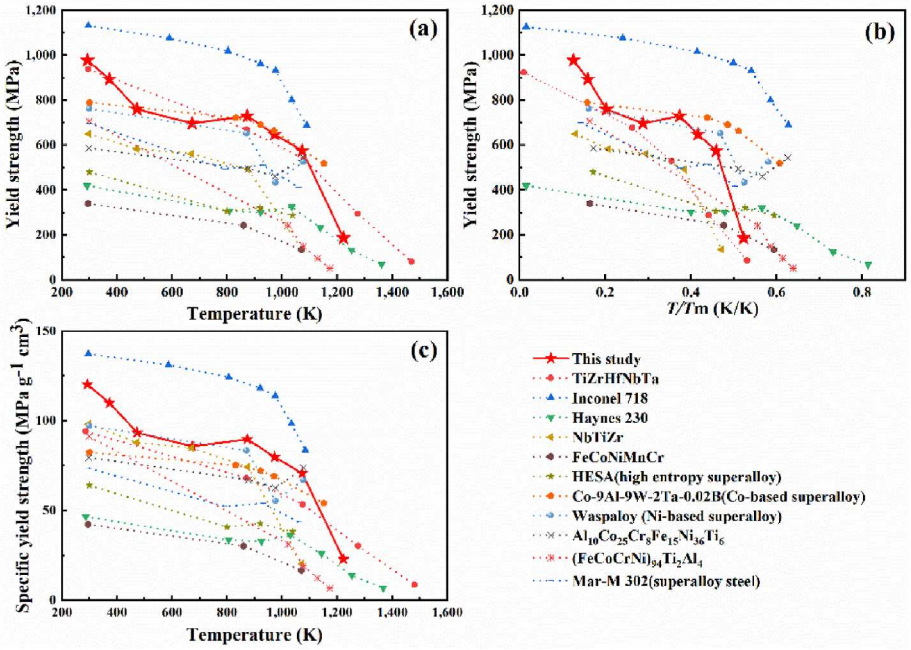

Fig. 4. Mechanical properties of the $Ti_{37}V_{15}Nb_{22}Hf_{23}W_3$ RHEA. (a, b) Yield strength as a function of the testing temperature and homologous temperature (T/T_m) under tension with other superalloys. (c) Specific yield strength as a function of the testing temperature of the CrMoNbV alloy under tension with other superalloys.

the $Ti_{37}V_{15}Nb_{22}Hf_{23}W_3$ alloy is not excellent. The traditional Inconel 718 superalloy exhibits superior excellent high-temperature mechanical properties [1,48]. However, the Inconel 718 alloy requires complex heat treatments to ensure its mechanical properties and corrosion resistance [51,52]. The as-cast $Ti_{37}V_{15}Nb_{22}Hf_{23}W_3$ alloy possesses a unique advantage between 298 and 1073 K. Specifically, the specific strength of this alloy is significantly superior to that of other superalloys, as demonstrated in Fig. 4(c).

Fig. 5 presents the inverse pole figure (IPF) and kernel average misorientation (KAM) of tensile samples at different temperatures. The high-temperature tensile sample is a single-phase solid solution, and the grain size is approximately 20–40 μm. The difference in grain sizes is

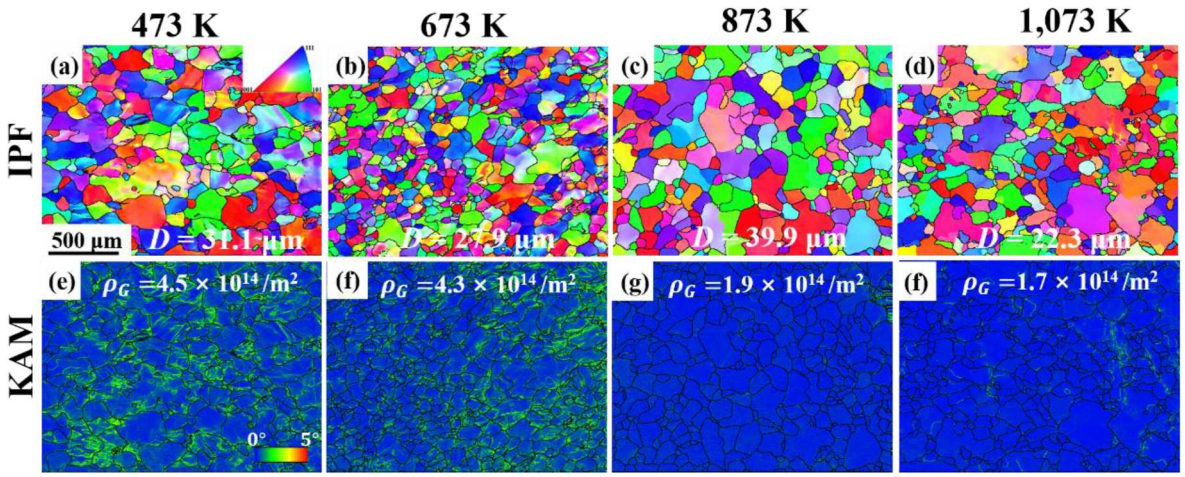

Fig. 5. (a–d) EBSD IPF maps and corresponding grain size of different temperatures; and (e–f) EBSD KAM maps and corresponding dislocation densities.

more likely to result from the randomness of the sample rather than the coarsening of the grains. This trend indicates that none of samples underwent phase transformation or twinning during the high-temperature deformation and the dislocation movement undertakes the plastic deformation of the samples [53–55]. The KAM value calculates the average misorientation between a pixel, *i*, and its neighbors, assuming that the misorientation does not exceed a given threshold value (usually 5°). The hue, ranging from blue to red, reflects the KAM value in the 0–5° range. The low-temperature sample exhibits a higher misorientation, as indicated by the presence of numerous green lines in the KAM map, as shown in Fig. 5(e). As the temperature of the tests increases, the proportion of green lines gradually decreases. In Fig. 5(f), when the temperature is increased to 1073 K, the color of the KAM map appears predominnantly almost blue. The geometrically necessary dislocation density (ρ_{GND}) can be quantified using the formula [17,56].

$$\rho_{GND} = \frac{2\theta_{KAM}}{xb} \tag{2}$$

where x is the unit length, which is the step size of the scan (10^{-5} /m), θ_{KAM} is Kernel average misorientation obtained, using graphs displayed in Fig. 5(e–h), and b is the Burgers vector of the dislocation slip. As presented in Fig. 2, the ρ_{GND} of the alloy is steadily decreased with increasing the testing temperature, and this change trend is consistent with the ductility of the tensile sample. This feature indicates that the plastic deformation of the current alloy is closely related to the proliferation of dislocations, which results in an increase in the dislocation density of the alloy, indicating that the deformation mechanism may be primarily associated with dislocation slip [57,58].

Fig. 6 provides an impression of misorientation distributions of the $Ti_{37}V_{15}Nb_{22}Hf_{23}W_3$ RHEA at different temperatures. At 473 and 673 K, the majority of grain boundaries are the low-angle grain boundaries (LAGBs), while at 873 and 1073 K, the majority are the high-angle grain boundaries (HAGBs). The tensile ductility of the $Ti_{37}V_{15}Nb_{22}Hf_{23}W_3$ alloy is noticeably impacted by this large evolution of GB types. Rupp et al. [59] concluded that cracks under stress loading conditions

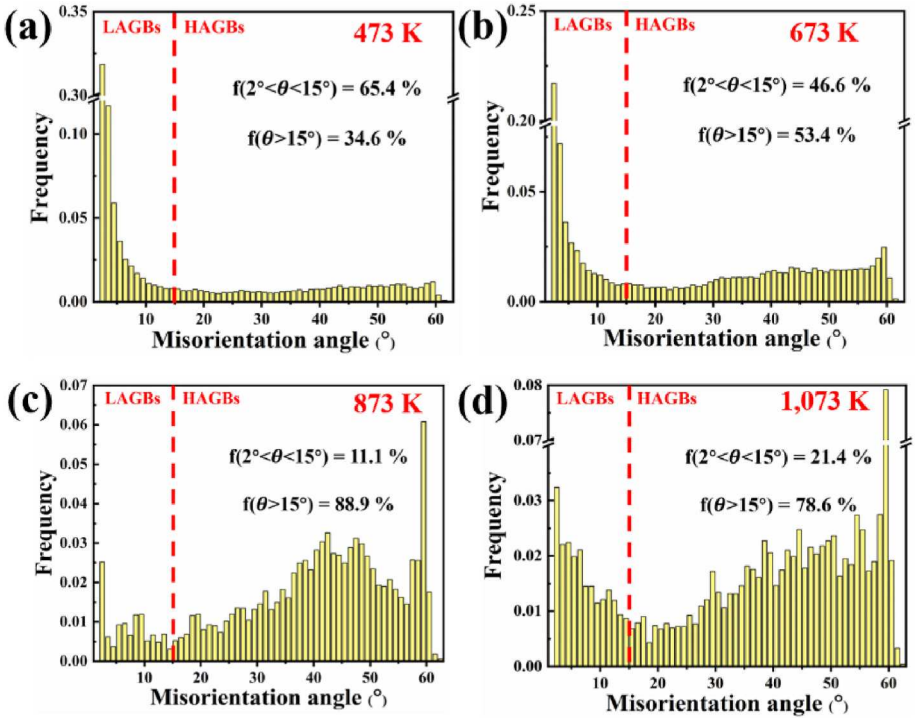

Fig. 6. Misorientation angle obtained from EBSD results of the $Ti_{37}V_{15}Nb_{22}Hf_{23}W_3$ RHEA at different temperature: (a) 473 K, (b) 673 K, (c) 873 K, and (d) 1073 K.

propagate along HAGBs and result in brittle fracture of the alloy along the intergranular region. Similar conclusions were obtained by Terentyev et al. [60], who concluded that the increased LABGs has a shielding and passivating effect on the crack points, thereby improving the tensile ductility. The stress-strain curve, given in Fig. 2(a), confirms this trend. LAGBs have stronger fracture resistance than HAGBs, and it has long been recognized that the intergranular strain compatibility of LAGBs is better than that of HAGBs [61]. The simulation results also indicate that LAGBs efficiently decrease the need for independent slip systems in BCC crystals and may transmit strains across grains without fracture [62]. The findings of three-point bending tests indicate that LAGBs have stronger fracture resistance than HAGBs [63]. As a result, the large fraction of LAGBs greatly reduces strain incompatibility, enhancing the ductility of the BCC $Ti_{37}V_{15}Nb_{22}Hf_{23}W_3$ RHEA. According to the crystallographic study, weak lattice coherency in HAGBs impedes dislocation migration, leading to the accumulation and entanglement of dislocations, which have been identified as sites where cracks initiate [42]. On the other hand, the orientation difference of the LAGBs in the $Ti_{37}V_{15}Nb_{22}Hf_{23}W_3$ alloy is less than 15°, i.e., the lattice on both sides of the LAGBs is more coherent, allowing slip dislocations to pass through the LAGBs more effectively, rather than getting blocked on one side of the LAGBs. As stated by Clark et al. and Birnbaum et al. [64,65], the most favorable selection rule for dislocation transfer is when the grain boundaries are parallel to both the slip plane and direction. Additionally, when the slip planes are not parallel, it is important to minimize the angle (θ) between the inlet and outlet slip planes. According to the selection guidelines [64,65], LAGBs provide a better pathway for transboundary slip of the dislocation than HAGBs, dislocations to move across borders, while also avoiding the stress concentration at GBs. Misra et al. [66,67] observed similar results in tests of interphase boundaries, suggesting that the effective slip transmission plays a significant role in the outstanding ductility of Ni–Fe–Al alloys at room temperature. Furthermore, in LAGBs, dislocation network segments finction as Frank-Read sources, serving as locations for dislocation nucleation and delayed fracture [68]. Increased LAGBs have two primary favorable impacts on the dislocation emission: (i) dislocation nucleation, and subsequently (ii) dislocation gliding, which enhance the ductility of the present $Ti_{37}V_{15}Nb_{22}Hf_{23}W_3$ alloy.

The microstructures of $Ti_{37}V_{15}Nb_{22}Hf_{23}W_3$ RHEA specimens undergoing tensile deformation at various temperatures until fracture are investigated using TEM (Fig. 7). The dislocation morphology indicated cross-kinks/jogs (edge-dipoles) on screw dislocations at 473 K and 673 K [Fig. 7(a and b)]. Very long and straight screw dislocations were found at 473 K [Fig. 7(a_2)]. Furthermore, TEM analysis demonstrated that the deformation occurred only through dislocation slip, as there was no evidence of deformation twinning. At 673 K, the TEM image revealed a denser and complex dislocation structure (containing a large number of dislocation debris and loops), causing it to become challenging to distinguish individual dislocation structures [Fig. 7(b_2)]. At higher temperatures (873 K), the microstructure consisted of dislocation slip bands and numerous dislocation fragments (dipoles and jogs), similar to those observed at 473 K and 673 K [Fig. 7(c-c_2)]. When the temperature rises further (1,073 K), the microstructure changes dramatically [Fig. 7 (d-d_2)]. The dislocation density is reduced, and there are no dislocation loops or dislocation fragments [Fig. 7(d-d_2)]. This trend implies that the dislocations lack cross-kinks, which is different from the morphologies of the dislocations observed at lower deformation temperatures. The low dislocation density confirms the low fracture elongation (Fig. 2). Inverse fast Fourier transform (FFT) plots and high-resolution transmission electron microscopy (HRTEM) images of the $Ti_{37}V_{15}Nb_{22}Hf_{23}W_3$ RHEA after tensile fracture at various temperatures are shown in Fig. 8(a–c). Severe plastic deformation introduces a large number of dislocations, and this abundance of dislocations causes a lattice mismatch in the crystal, which in turn leads to the bending of dislocation lines in the FFT.

Fig. 9 depicts the TEM characterization and dislocation type analysis of the $Ti_{37}V_{15}Nb_{22}Hf_{23}W_3$ RHEA after tensile fracture at 673 K. No

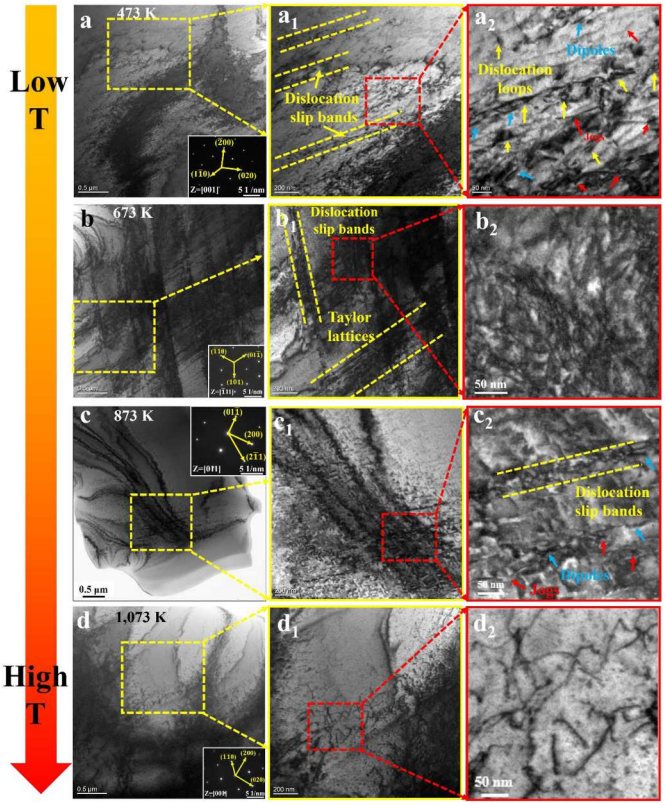

Fig. 7. TEM bright-field image of the deformed sample of the $Ti_{37}V_{15}Nb_{22}Hf_{23}W_3$ RHEA under $\varepsilon = 0.001/s$ at different temperatures: (a) 473 K, (b) 673 K, (c) 873 K, and (d) 1073 K.

twinning, stacking faults, or phase transitions were found in the alloy before or after the tensile fracture. Instead, a significant number of slip dislocations were observed. This suggests that the dislocation slip in the alloy at 673 K is responsible for all the plastic deformation (see Figs. 7(b) and Fig. 9(b)). To determine the Burgers vector of the dislocations, the dislocation features were characterized by TEM under two-beam conditions (Fig. 9(b–e)). The TEM contrast of a dislocation is related to $\boldsymbol{g} \bullet \boldsymbol{b}$, and when $|\boldsymbol{g} \bullet \boldsymbol{b}|/gb > 1/3$, the contrast is visible in the TEM image. Fig. 9(h) summarizes relevant the possible combinations of Burgers vectors and their contrasts with respect to the $\boldsymbol{g}$ vectors that were $[\bar{2}00]$, $[01\bar{1}]$, $[\bar{2}1\bar{1}]$, and $[22\bar{2}]$, which were selected for the investigation. It is always known that the <111> type represents the well-established Burgers vector in elemental and dilute BCC alloys. For both Burgers vectors, [111] and $[\bar{1}\ 11]$, have the same contrast conditions and so they cannot be distinguished. They presented dislocation contrasts for $\boldsymbol{g}$ of [200] and $[2\ \bar{1}\ 1]$, and invisibility for $[01\bar{1}]$ and $[22\ \bar{2}]$. For Burgers vectors of $[1\ \bar{1}\ 1]$ and $[11\bar{1}]$, they have no contrast only under one $\boldsymbol{g}$ vectors respectively. Furthermore, not all dislocations are visible under the $\boldsymbol{g} = [22\bar{2}]$ vector. Based on these various conditions, we can interpret the TEM data, which shows dislocation contrasts for the different imaging conditions ($\boldsymbol{g}$ vectors). In Fig. 9 (a), an area is selected, where the dislocation line is clearly visible for the specified dislocation type, as depicted in Fig. 9 (f). The 30 dislocation lines were identified (Fig. 9(f and g)), and the Burgers vector of the dislocation was determined according to whether the dislocation was visible or not visible under different $\boldsymbol{g}$ vectors. The vectors of the 30 dislocation lines ($\boldsymbol{\xi}$) in Fig. 9 (g) are determined using stereographic projection (Fig. 9 (i)) [26]. The identification results of these dislocation line vectors ($\boldsymbol{\xi}$) are shown in Table 2. Furthermore, the type of dislocation (edge or screw) can be determined by examining the relationship between the dislocation line vector ($\boldsymbol{\xi}$) and the Burgers vector ($\boldsymbol{b}$). For example, if $\boldsymbol{\xi}$ is perpendicular

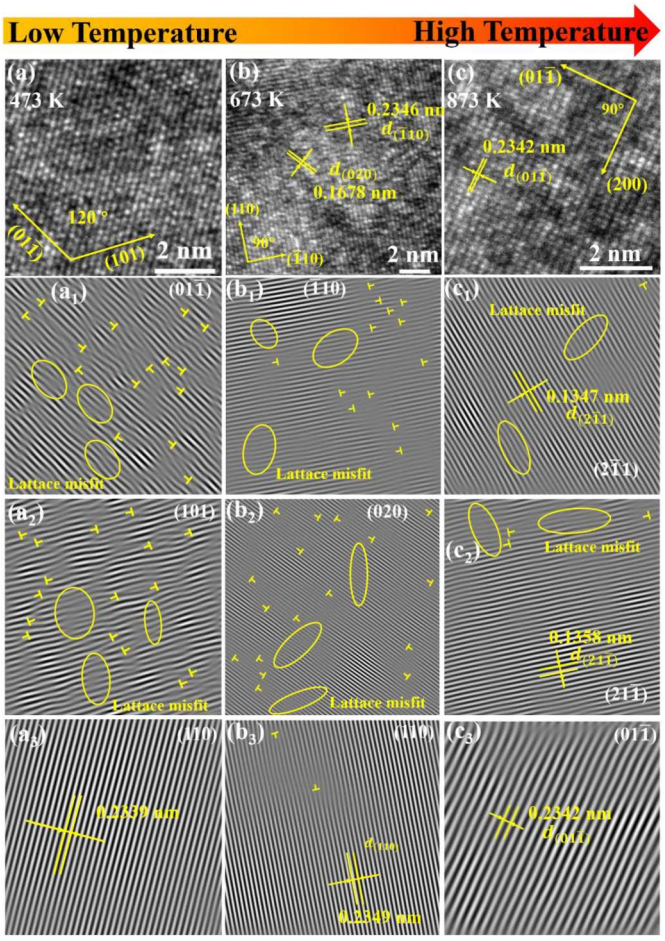

Fig. 8. Lattice-uniformity analysis of the $Ti_{37}V_{15}Nb_{22}Hf_{23}W_3$ RHEA after tensile fracture at different temperatures and the corresponding Inversed Fast Fourier Transform (FFT) images.

to ***b***, the dislocation line is an edge dislocation; if ***ξ*** is parallel to ***b***, the dislocation line is a screw dislocation. The results for the angle between ***ξ*** and ***b*** in the 30 dislocation lines of Fig. 9(g) are presented in Table 2. Most dislocations are mixed dislocations. Furthermore, there were 7 dislocations more inclined to edge dislocations and 23 dislocations more inclined to screw dislocations (see Fig. 9(i) and Table 2). Based on a similar method as described above, the dislocation type of the $Ti_{37}V_{15}Nb_{22}Hf_{23}W_3$ RHEA after tensile fracture at 873 K was counted and is shown in Fig. 10. The details of the 30 dislocation lines in Fig. 10 (g) are shown in Table 3. If 45° is used as the "standard" for determining the edge dislocation or screw dislocation. Then, in Fig. 10(g), there are 17 dislocations that tend to be edge dislocations and 13 dislocations that tend to be screw dislocations. Among the dislocation types observed in the $Ti_{37}V_{15}Nb_{22}Hf_{23}W_3$ RHEA after tensile fracture at 1073 K, 14 dislocation lines are classified as edge dislocations, while only one dislocation line exhibits characteristics of a screw dislocation (Fig. 11).

4. Discussion

4.1. Brittle fracture at high temperature

At testing temperatures of 298 and 1223 K, the $Ti_{37}V_{15}Nb_{22}Hf_{23}W_3$ RHEA exhibited high tensile ductility (~20 % and ~40 %, respectively). At 1073 K, the $Ti_{37}V_{15}Nb_{22}Hf_{23}W_3$ RHEA displayed considerably reduced ductility (2 %), which corresponded to a transition from ductile to intergranular fracture. This trend may come from the following three reasons: (i) ductile to brittle transition (DBT) [22,69,70], (ii) high-temperature oxidation [71], and (iii) precipitated phase at high temperatures [30].

(i) DBT characteristics of BCC alloys. DBT means that the toughness of BCC metallic materials decreases with reducing temperatures, from a ductile to brittle fracture transition [72,73]. The tensile ductility of the BCC $Ti_{37}V_{15}Nb_{22}Hf_{23}W_3$ RHEA in this study is about 20 % at room temperature. According to the definition of DBT, the ductile to brittle transition temperature (DBTT) must be below the room temperature. It also means that the reason for brittle fracture at 1073 K must not be that the alloy has undergone a ductile-brittle transition. This feature would rule out the reason.

(ii) High-temperature oxidation during the tensile process. When tested at 1073 K, the embrittlement element of oxygen from the environment can quickly permeate along the GBs, lowering their cohesiveness and causing an easy start of intergranular cracking [71,74]. This similar dynamic oxygen embrittlement behavior has been reported in the literature [75]. However, it is difficult to observe impurities formed due to oxidation from the SEM images of the fracture surface (Fig. 3(f)).

(iii) Precipitation at high temperatures. The significant drop in ductility at 1073 K is similar to that found in the TiZrHfNbTa alloy [30]. It was reported that it was due to the formation of two different precipitates at the grain boundaries within a heating time as short as 6 min [30]. Precipitation at grain boundaries played an important role in the transition from the ductile to intergranular fracture [30]. However, Fig. 7(d) shows a single-phase BCC structure, and no precipitates were observed.

In order to further identify the cause for the significant decrease in toughness at 1,073 K, we sealed the as-cast sample in a quartz tube, heat-treated it at 1,073 K for 15 min, and then quenched it into the water. The room-temperature uniaxial tensile stress-strain curve is shown in Fig. 12 (a). A transition from the plastic to brittle fracture was found. It is believed that the brittle fracture of the 1,073 K uniaxial tensile specimen was due to precipitation at the grain boundaries during heating times as short as 15 min. These precipitates are not only scarce, but also extremely small, possibly only a few nanometers in size. Consequently, locating these sporadic precipitates dispersed along grain boundaries within a limited field of view in the TEM is a significant challenge.

4.2. The transition from screw dislocation to edge dislocation at high temperatures

The motion of screw dislocations in BCC metals or dilute BCC alloys is well-established to control yield strength [22,25]. The motion of edge dislocation is almost universally ignored. For multi-principal RHEAs, the broad dispersion of slip resistance due to chemical fluctuations at the atomic level leads to the multiplicity of dislocation pathways, which differs from the dislocation slip behavior in conventional BCC metals [76]. Recent studies of RHEAs provide an evidence of the increasing importance of edge dislocations. For instance, the edge dislocation is prodominant at the beginning of the plastic flow in TiZrHfNbTa alloy [24]. Feng et al. [1] found that edge dislocations play an important role in the superior high-temperature strength of CrMoNbV RHEA. Lee et al. [26]. were more directly suggesting that edge dislocations control the strength of RHEAs. This experiment also partially confirmed the above views. At different temperatures, the edge dislocations play different roles (Figs. 9–11). At 673 K, there were only 7 edge dislocations out of the 30 dislocation lines (see Fig. 9(g) and Table 2). When the temperature was raised to 873 K, there were 17 edge dislocations out of 30 dislocation lines (see Fig. 10(g) and Table 3). As the temperature increases, the number of edge dislocations increases significantly, while the proportion of screw dislocations becomes more significant (~40 %), as shown in Fig. 13. It is similar to Feng et al. [1], but inconsistent with

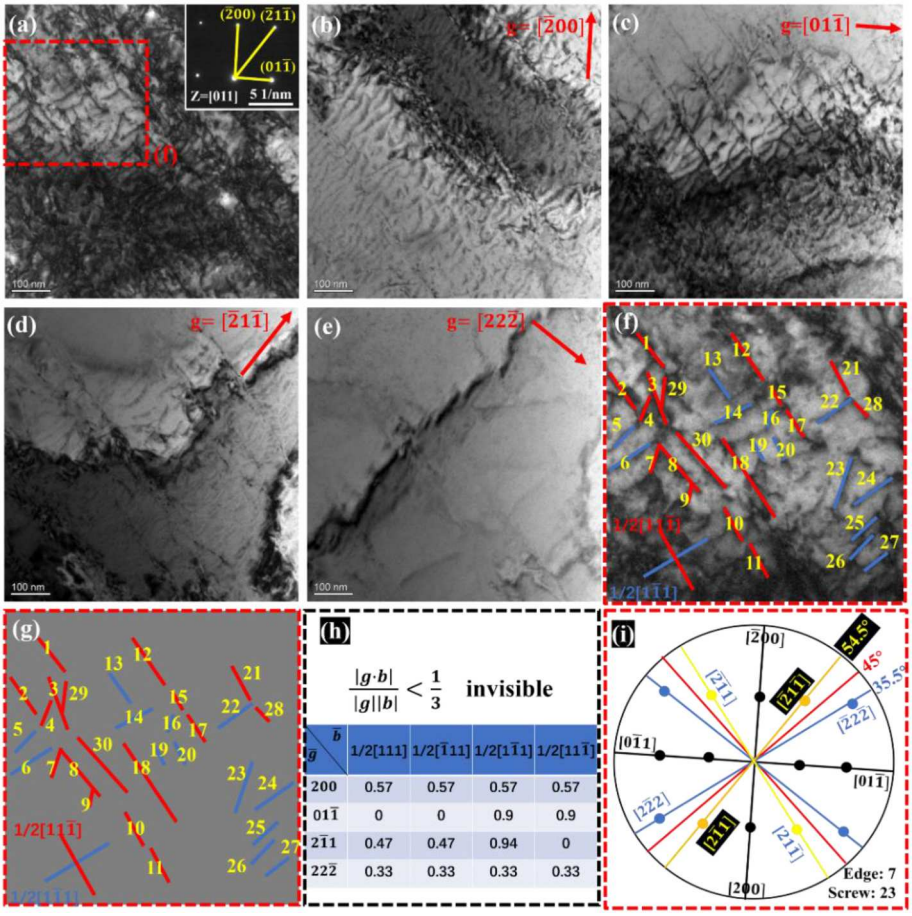

g \ b	1/2[111]	1/2[$\bar{1}$11]	1/2[1$\bar{1}$1]	1/2[11$\bar{1}$]
200	0.57	0.57	0.57	0.57
01$\bar{1}$	0	0	0.9	0.9
2$\bar{1}$1	0.47	0.47	0.94	0
22$\bar{2}$	0.33	0.33	0.33	0.33

Fig. 9. The TEM characterization and dislocation type analysis for the $Ti_{37}V_{15}Nb_{22}Hf_{23}W_3$ RHEA after tensile fracture at 673 K. (a) The bright field TEM images and SAED analysis. (b–e) The two-beam bright field TEM images of the dislocations of the deformed sample at 673 K with different **g** vectors along the zone axes of [011]. The **g** vector is annotated in each image with the direction shown by the red arrow. (f) An enlarged dislocations region of the boxed area in (a). The Bugers vectors are determined from the projected cubic lattice, with the red line and blue line denoting $1/2[11\bar{1}]$ and $1/2[1\bar{1}1]$, respectively. (g) A schematic presents the dislocation lines marked in (f), in which the dislocations numbered 1–30 for the dislocation-line-direction analysis. The dislocations are colored according to their respective Burgers vectors. (h) Normalized **g·b** values for possible Burgers vectors under the imaging conditions used in (g). Absolute values of $\frac{|g\bullet b|}{|g\bullet b|} < \frac{1}{3}$ are invisible. (i) Stereographic projection related to the [011] orientation, which determined the relationship among all possible dislocation lines $\boldsymbol{\xi}$ in (g) and the Burger vector $\boldsymbol{b}$. If $\boldsymbol{\xi}$ is parallel to $\boldsymbol{b}$, the type of dislocation is a screw dislocation. The types of daily dislocation lines in (g) shown in Table 2. (For interpretation of the references to color in this figure legend, the reader is referred to the Web version of this article.)

Table 2
Types of dislocations of the $Ti_{37}V_{15}Nb_{22}Hf_{23}W_3$ RHEA after fracture at 673 K.

No.	$\boldsymbol{\xi}$	$\boldsymbol{b}$	$cos^{-1}(\boldsymbol{\xi}\bullet\boldsymbol{b})$	Type	No.	$\boldsymbol{\xi}$	$\boldsymbol{b}$	$cos^{-1}(\boldsymbol{\xi}\bullet\boldsymbol{b})$	Type
1	[85$\bar{5}$]	[11$\bar{1}$]	13°	Screw	16	[$\bar{4}$1$\bar{1}$]	[1$\bar{1}$1]	35°	Screw
2	[21$\bar{1}$]	[11$\bar{1}$]	19°	Screw	17	[21$\bar{1}$]	[11$\bar{1}$]	19°	Screw
3	[53$\bar{3}$]	[11$\bar{1}$]	14°	Screw	18	[21$\bar{1}$]	[11$\bar{1}$]	19°	Screw
4	[4$\bar{1}$1]	[11$\bar{1}$]	74°	Edge	19	[21$\bar{1}$]	[1$\bar{1}$1]	90°	**Edge**
5	[2$\bar{1}$1]	[1$\bar{1}$1]	19°	Screw	20	[21$\bar{1}$]	[1$\bar{1}$1]	90°	**Edge**
6	[2$\bar{1}$1]	[1$\bar{1}$1]	19°	Screw	21	[21$\bar{1}$]	[11$\bar{1}$]	19°	Screw
7	[6$\bar{1}$1]	[11$\bar{1}$]	68°	**Edge**	22	[$\bar{2}$2$\bar{2}$]	[1$\bar{1}$1]	0°	Screw
8	[32$\bar{2}$]	[11$\bar{1}$]	11°	Screw	23	[$\bar{4}$1$\bar{1}$]	[1$\bar{1}$1]	35°	Screw
9	[200]	[11$\bar{1}$]	55°	**Edge**	24	[$\bar{2}$2$\bar{2}$]	[1$\bar{1}$1]	0°	Screw
10	[21$\bar{1}$]	[11$\bar{1}$]	19°	Screw	25	[$\bar{2}$1$\bar{1}$]	[1$\bar{1}$1]	19°	Screw
11	[21$\bar{1}$]	[11$\bar{1}$]	19°	Screw	26	[$\bar{2}$1$\bar{1}$]	[1$\bar{1}$1]	19°	Screw
12	[21$\bar{1}$]	[11$\bar{1}$]	19°	Screw	27	[$\bar{2}$2$\bar{2}$]	[1$\bar{1}$1]	0°	Screw
13	[21$\bar{1}$]	[1$\bar{1}$1]	90°	**Edge**	28	[43$\bar{3}$]	[11$\bar{1}$]	2°	Screw
14	[$\bar{4}$55]	[1$\bar{1}$1]	6°	Screw	29	[200]	[11$\bar{1}$]	55°	**Edge**
15	[21$\bar{1}$]	[11$\bar{1}$]	19°	Screw	30	[32$\bar{2}$]	[11$\bar{1}$]	11°	Screw

Lee et al. [26]. When the temperature reaches 1073 K, there are 14 edge dislocation lines out of 15 dislocations, and the remaining dislocation is a mixed dislocation (see Fig. 11(g) and Table 4). At this point, the edge dislocation is responsible for almost all the plastic deformation of the alloy. Fig. 13 shows the proportion and ratio of dislocation types after tensile fracture of the $Ti_{37}V_{15}Nb_{22}Hf_{23}W_3$ RHEA at different

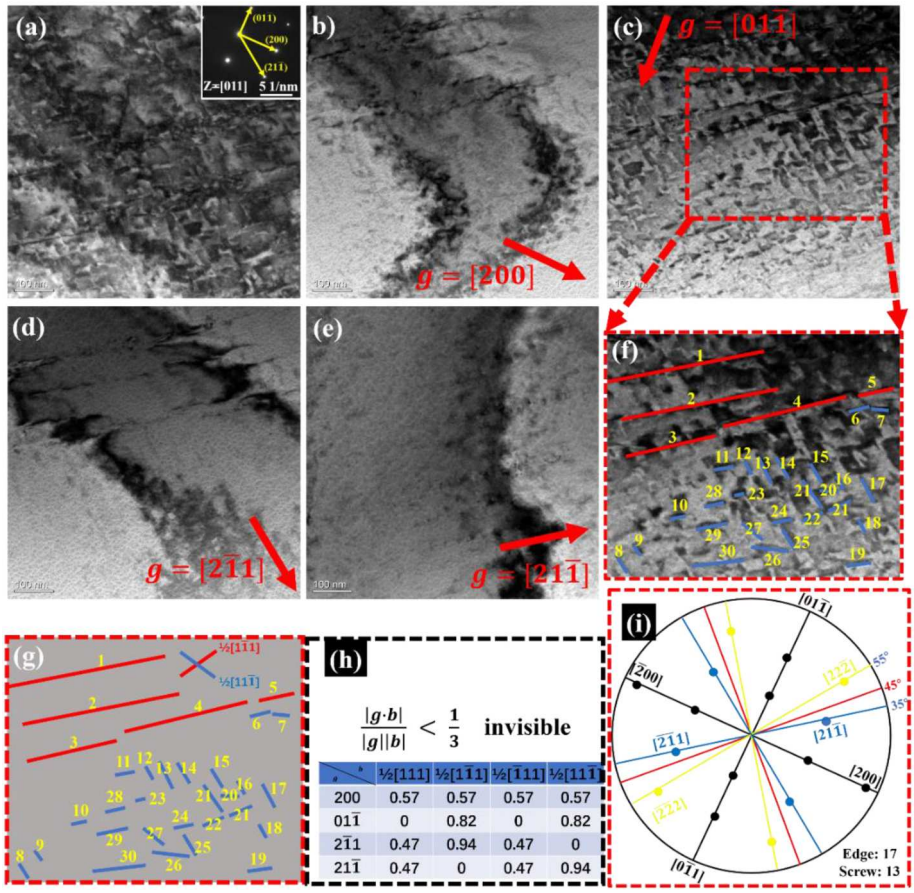

g \ b	½[111]	½[1$\bar{1}$1]	½[$\bar{1}$11]	½[11$\bar{1}$]
200	0.57	0.57	0.57	0.57
01$\bar{1}$	0	0.82	0	0.82
2$\bar{1}$1	0.47	0.94	0.47	0
21$\bar{1}$	0.47	0	0.47	0.94

Fig. 10. The TEM characterization and dislocation type analysis for the $Ti_{37}V_{15}Nb_{22}Hf_{23}W_3$ RHEA after tensile fracture at 873 K. (a) The bright field TEM images and SAED analysis. (b–e) The two-beam bright field TEM images of the dislocations feature of deformed sample at 873 K with different **g** vectors along the zone axes of [011]. The **g** vector is annotated in each image with the direction shown by the red arrow. (f) An enlarged dislocations region of the boxed area in (c). The Bugers vectors are determined from the projected cubic lattice, with the red line and blue line denoting $1/2[1\bar{1}1]$ and $1/2[11\bar{1}]$, respectively. (g) A schematic presents the dislocation lines marked in (f), in which the dislocations numbered 1–30 for the dislocation-line-direction analysis. The dislocations are colored according to their respective Burgers vectors. (h) Normalized **g**·**b** values for possible Burgers vectors under the imaging conditions used in (g). Absolute values of $\frac{|g\bullet b|}{|g|\bullet|b|} < \frac{1}{3}$ are invisible. (i) Stereographic projection related to the [011] orientation, which determined the relationship between all possible dislocation lines $\boldsymbol{\xi}$ in (g) and the Burger vector $\boldsymbol{b}$. If $\boldsymbol{\xi}$ is parallel to $\boldsymbol{b}$, the type of dislocation is a screw dislocation. The types of daily dislocation lines in (g) are shown in Table 3. (For interpretation of the references to color in this figure legend, the reader is referred to the Web version of this article.)

Table 3
Types of dislocations of the $Ti_{37}V_{15}Nb_{22}Hf_{23}W_3$ RHEA after fracture at 873 K.

No.	$\boldsymbol{\xi}$	$\boldsymbol{b}$	$cos^{-1}(\boldsymbol{\xi}\bullet\boldsymbol{b})$	Type	No.	$\boldsymbol{\xi}$	$\boldsymbol{b}$	$cos^{-1}(\boldsymbol{\xi}\bullet\boldsymbol{b})$	Type
1	[11$\bar{1}$]	[1$\bar{1}$1]	71°	**Edge**	16	[2$\bar{1}$1]	[11$\bar{1}$]	90°	**Edge**
2	[11$\bar{1}$]	[1$\bar{1}$1]	71°	**Edge**	17	[2$\bar{1}$1]	[11$\bar{1}$]	90°	**Edge**
3	[11$\bar{1}$]	[1$\bar{1}$1]	71°	**Edge**	18	[2$\bar{1}$1]	[11$\bar{1}$]	90°	**Edge**
4	[11$\bar{1}$]	[1$\bar{1}$1]	71°	**Edge**	19	[11$\bar{1}$]	[11$\bar{1}$]	0°	Screw
5	[11$\bar{1}$]	[1$\bar{1}$1]	71°	**Edge**	20	[41$\bar{1}$]	[11$\bar{1}$]	36°	Screw
6	[11$\bar{1}$]	[11$\bar{1}$]	0°	Screw	21	[2$\bar{1}$1]	[11$\bar{1}$]	90°	**Edge**
7	[41$\bar{1}$]	[11$\bar{1}$]	36°	Screw	22	[11$\bar{1}$]	[11$\bar{1}$]	0°	Screw
8	[2$\bar{1}$1]	[11$\bar{1}$]	90°	**Edge**	23	[11$\bar{1}$]	[11$\bar{1}$]	0°	Screw
9	[2$\bar{1}$1]	[11$\bar{1}$]	90°	**Edge**	24	[11$\bar{1}$]	[11$\bar{1}$]	0°	Screw
10	[11$\bar{1}$]	[11$\bar{1}$]	0°	Screw	25	[2$\bar{1}$1]	[11$\bar{1}$]	90°	**Edge**
11	[11$\bar{1}$]	[11$\bar{1}$]	0°	Screw	26	[41$\bar{1}$]	[11$\bar{1}$]	36°	Screw
12	[2$\bar{1}$1]	[11$\bar{1}$]	90°	**Edge**	27	[4$\bar{1}$1]	[11$\bar{1}$]	66°	**Edge**
13	[2$\bar{1}$1]	[11$\bar{1}$]	90°	**Edge**	28	[11$\bar{1}$]	[11$\bar{1}$]	0°	Screw
14	[2$\bar{1}$1]	[11$\bar{1}$]	90°	**Edge**	29	[11$\bar{1}$]	[11$\bar{1}$]	0°	Screw
15	[2$\bar{1}$1]	[11$\bar{1}$]	90°	**Edge**	30	[21$\bar{1}$]	[11$\bar{1}$]	19°	Screw

temperatures. As the tensile temperature of the sample increases from 673 K to 1073 K, the proportion of edge dislocations gradually increases, from ~20 % up to ~90 %. In other words, as the temperature increases, the type of dislocation responsible for the plastic deformation of the alloy gradually shifts from screw dislocation to edge dislocation.

It is generally believed that the plastic deformation of BCC metals is primarily dominated by screw dislocations. The screw dislocation of BCC metals has a three-dimensional core structure, as illustrated in

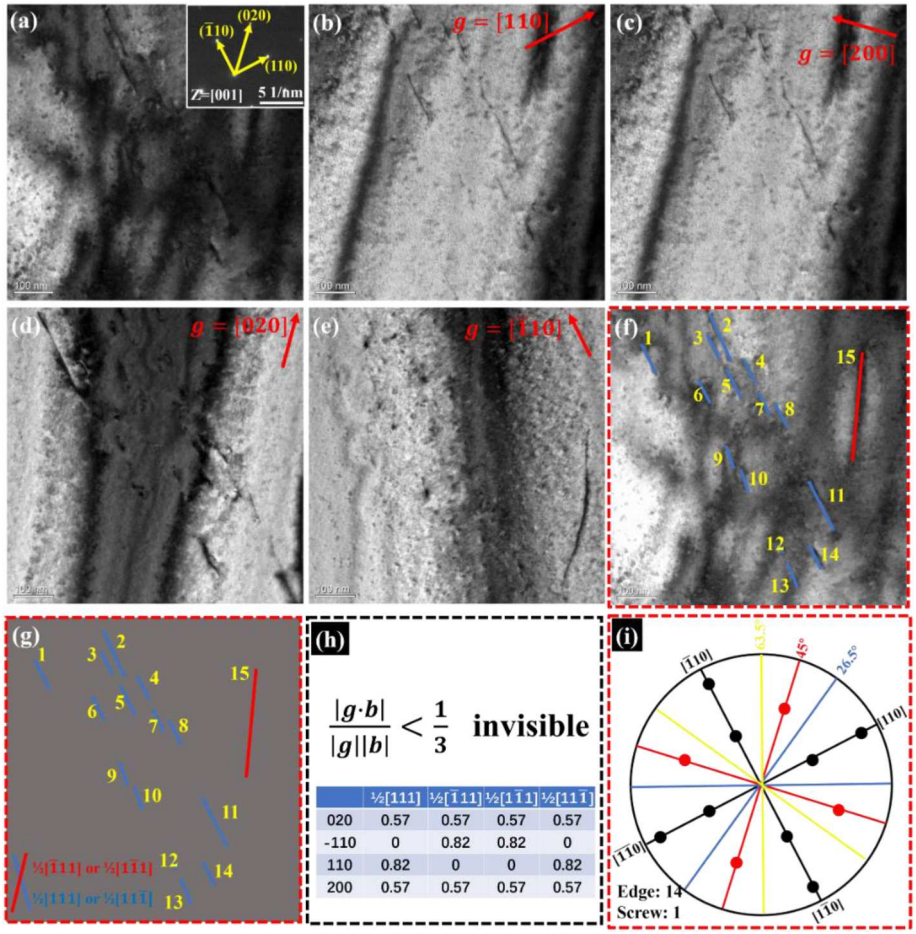

	½[111]	½[1̄11]	½[1 1̄ 1]	½[11 1̄]
020	0.57	0.57	0.57	0.57
-110	0	0.82	0.82	0
110	0.82	0	0	0.82
200	0.57	0.57	0.57	0.57

Fig. 11. The TEM characterization and dislocation type analysis for the $Ti_{37}V_{15}Nb_{22}Hf_{23}W_3$ RHEA after tensile fracture at 1073 K. (a) The bright field TEM images and SAED analysis. (b–e) The two-beam bright field TEM images of the dislocations feature of deformed sample at 1073 K with different **g** vectors along the zone axes of [001]. The **g** vector is annotated in each image with the direction shown by the red arrow. (f) The dislocation lines are marked in (a). The Bugers vectors are determined from the projected cubic lattice, with the red line and blue line denoting $1/2[1\bar{1}1]$ (or $1/2[\bar{1}11]$) and $1/2[11\bar{1}]$ (or $1/2[111]$), respectively. (g) A schematic presents the dislocation lines marked in (f), in which the dislocations numbered 1–15 for the dislocation-line-direction analysis. The dislocations are colored according to their respective Burgers vectors. (h) Normalized **g**·**b** values for possible Burgers vectors under the imaging conditions used in (g). Absolute values of $\frac{|g\bullet b|}{|g|\bullet|b|} < \frac{1}{3}$ are invisible. (i) Stereographic projection related to the [001] orientation, which determined the relationship between all possible dislocation lines $\boldsymbol{\xi}$ in (g) and the Burger vector $\boldsymbol{b}$. If $\boldsymbol{\xi}$ is parallel to $\boldsymbol{b}$, the type of dislocation is a screw dislocation. The types of daily dislocation lines in (g) shown in Table 4. (For interpretation of the references to color in this figure legend, the reader is referred to the Web version of this article.)

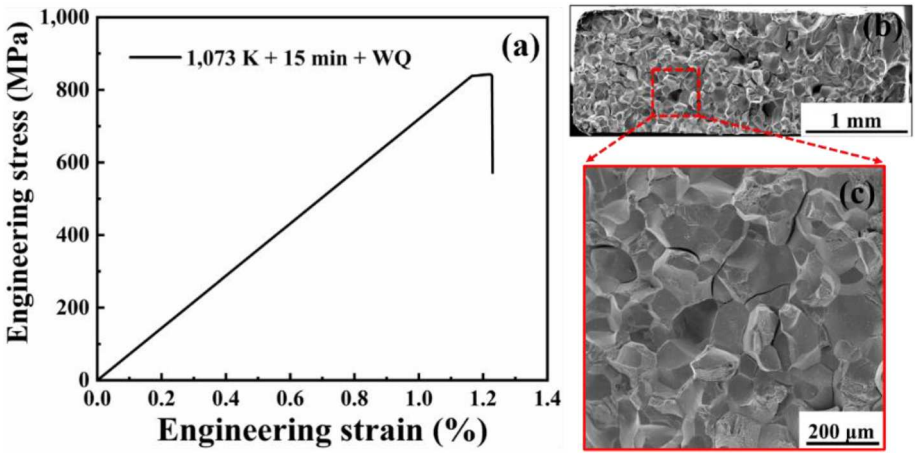

Fig. 12. (a)The room-temperature uniaxial tensile test of the $Ti_{37}V_{15}Nb_{22}Hf_{23}W_3$ RHEA after the heat treatment at 1073 K for 15 min; (b–c) Secondary electron (SE) SEM micrographs of the fracture surfaces reveal the failure modes of the sample, following tensile loading.

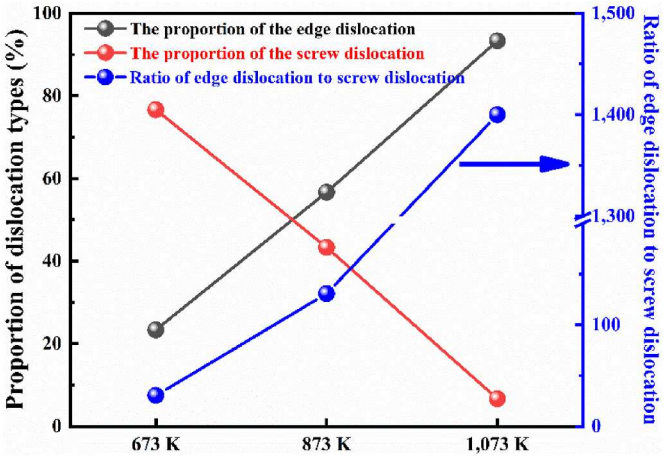

Fig. 13. The proportion and ratio of dislocation types after tensile fracture of the $Ti_{37}V_{15}Nb_{22}Hf_{23}W_3$ RHEA at different temperatures.

Table 4
Types of dislocations of the $Ti_{37}V_{15}Nb_{22}Hf_{23}W_3$ RHEA after fracture at 1073 K.

No.	ξ	b	$cos^{-1}(\xi \bullet b)$	Type
1	$[1\bar{1}0]$	[111] or $[11\bar{1}]$	90°	**Edge**
2	$[1\bar{1}0]$	[111] or $[11\bar{1}]$	90°	**Edge**
3	$[1\bar{1}0]$	[111] or $[11\bar{1}]$	90°	**Edge**
4	$[1\bar{1}0]$	[111] or $[11\bar{1}]$	90°	**Edge**
5	$[1\bar{1}0]$	[111] or $[11\bar{1}]$	90°	**Edge**
6	$[1\bar{1}0]$	[111] or $[11\bar{1}]$	90°	**Edge**
7	$[1\bar{1}0]$	[111] or $[11\bar{1}]$	90°	**Edge**
8	$[1\bar{1}0]$	[111] or $[11\bar{1}]$	90°	**Edge**
9	$[1\bar{1}0]$	[111] or $[11\bar{1}]$	90°	**Edge**
10	$[1\bar{1}0]$	[111] or $[11\bar{1}]$	90°	**Edge**
11	$[1\bar{1}0]$	[111] or $[11\bar{1}]$	90°	**Edge**
12	$[1\bar{1}0]$	[111] or $[11\bar{1}]$	90°	**Edge**
13	$[1\bar{1}0]$	[111] or $[11\bar{1}]$	90°	**Edge**
14	$[1\bar{1}0]$	[111] or $[11\bar{1}]$	90°	**Edge**
15	$[1\bar{2}0]$	$[\bar{1}11]$ or $[1\bar{1}1]$	39°	Screw

Fig. 14(a). Project and observe the core of a screw dislocation along the Burgers vector <111> direction, where each point represents a column of atoms, and arrows represent the displacement difference between adjacent columns of atoms perpendicular to the paper direction [22]. Due to the special core structure of the screw dislocation of BCC metals, the simulation results indicate that the Peierls-Nabarro force required to initiate the screw dislocation at room temperature is at least one order of magnitude greater than that of the edge dislocation [77]. Therefore, compared with the edge dislocation, the movement of the screw dislocation is more difficult and requires larger thermal activation. The screw dislocation is ideally long and straight (see Fig. 14(b)). However, variations in composition and thermal activation in RHEAs can lead to the spontaneous formation of kinks in screw dislocations (Fig. 14(c)). The kinks move along the dislocation line under the action of stress (Fig. 14 (d)), thereby facilitating the slip of the screw dislocation [22]. Moreover, the slip deformation mechanism in BCC metals is fundamentally different from that of FCC metals: the slip plane is not unique, and the dislocation can slip in the {110}, {112} and {123} planes [72,78]. When kinks on different glide planes intersect, they form cross kinks (also known as jogs or dipoles) that act as strong pinning points [40], as shown in Fig. 14(e). Breaking the cross kink creates a high-energy point defect, which results in a high-energy flow barrier [40]. Therefore, as the temperatures increase, the more kinks will be caused by thermal activation, leading to the formation of more cross kinks under stress. The higher the energy required for high-temperature plastic deformation to break the cross kinks. At high temperatures, the motion of the screw dislocation becomes more challenging compared to that of the edge dislocation, or the slip rate of the screw dislocation is lower than that of the edge dislocation [40,79]. Therefore, more edge dislocations can be found at higher temperatures. That is to say, as the testing temperature increases, the slip pattern changes from screw dislocation to edge dislocation. This study just confirms this, with 23 % of the edge dislocations at 673 K (see Fig. 9). At 873 K, the percentage of edge dislocations was 57 % (Fig. 10). It continues to rise to 1,073 K, with almost all of them being edge dislocations (Fig. 11). This is the first demonstration of the evolution of dislocation types with the temperature in RHEAs.

4.3. The theory of strengthening for edge dislocations

Based on the analysis in section 4.2, the edge dislocation plays an important role in high-temperature strength. Starting from the motion of edge dislocation, Maresca et al. [25] established a thermal activation model for solid solution strengthening that is applicable at high temperatures. In the model, each alloyed element is treated as a solute that interacts with a dislocation in a hypothetical uniform "average" alloy that possesses all the macroscopic properties of a truly random alloy [26,80]. Fluctuations in the local arrangement of solutes lead to local changes in dislocation potential energy [25,80]. As a result, the dislocation spontaneously forms a wave structure to reduce energy to be adapt to the local solute environment. In addition, the plastic flow depends on the temperature and stress. A dislocation moving from a low-energy environment to an adjacent high-energy environment needs to overcome a significant barrier in the random alloys [25,26]. The intrinsic yield stress at a finite temperature (T) and a finite strain rate ($\dot{\varepsilon}$) is expressed as follows [25]:

$$\tau_y(T,\dot{\varepsilon}) = M\tau_{y0}\left[1-\left(\frac{kT}{\Delta E_b}ln\frac{\dot{\varepsilon}_0}{\dot{\varepsilon}}\right)^{\frac{2}{3}}\right], \tau_y \Big/ \tau_{y0} > 0.5 \quad (3)$$

$$\tau_y(T,\dot{\varepsilon}) = M\tau_{y0}\exp\left(-\frac{1}{0.55}\frac{kT}{\Delta E_b}ln\frac{\dot{\varepsilon}_0}{\dot{\varepsilon}}\right), \tau_y \Big/ \tau_{y0} < 0.5 \quad (4)$$

Here, $\dot{\varepsilon}_0 = 10^4/s$ is a reference strain-rate estimated [80]. $M = 2.76$ is the Taylor factor for polycrystalline BCC metals [76]. τ_{y0} is the zero-temperature shear yield stress. $k = 1.38 \times 10^{-23}$ J/K is the Boltzmann constant [1]. ΔE_b is the energy barrier for the thermal-activated at absolute zero.

$$\tau_{y0} = 0.04\alpha^{-\frac{1}{3}}G\left(\frac{1+\nu}{1-\nu}\right)^{\frac{4}{3}}\left[\frac{\sum_n c_n \Delta V_n^2}{b^6}\right]^{\frac{2}{3}} \quad (5)$$

$$\Delta E_{b0} = 2.0\alpha^{\frac{1}{3}}Gb^3\left(\frac{1+\nu}{1-\nu}\right)^{\frac{2}{3}}\left[\frac{\sum_n c_n \Delta V_n^2}{b^6}\right]^{\frac{1}{3}} \quad (6)$$

Here, $\alpha = 1/12$ is the weight coefficient of the dislocation line tension for the lattice of BCC structure. G is shear modulus, which is calculated using Vegard's law, and the calculation results are shown in Table 5. ν is Poisson's ratio, obtained from the formula $G = E/[2(1+\nu)]$, where E is calculated using Vegard's law (Table 6). The Burgers vector (b) of the $Ti_{37}V_{15}Nb_{22}Hf_{23}W_3$ RHEA is computed through $b = (\sqrt{3}a)/2$. The lattice constant (a) is 330.7 p.m., which comes from reference [27]. Applying Vegard's law to the average atomic volume of each solid solution, *i.e.* $\overline{V} = \sum_n c_n V_n$, with $V_n = a_n^3/2$, we calculte individual atomic volume (V_n) for each element (n), and get V_n = 17.58 Å^3, 14.03 Å^3, 17.98 Å^3, 22.54 Å^3, 15.75 Å^3 for Ti, V, Nb, Hf, and W, respectively. The misfit volume of an element (n) in the $Ti_{37}V_{15}Nb_{22}Hf_{23}W_3$ RHEA is estimated to be $\Delta V_n = V_n - \overline{V}$ (the sum rule $\sum_n c_n \Delta\overline{V}_n = 0$ is followed by construction).

Table 7 presents the experimental and predicted tensile yield

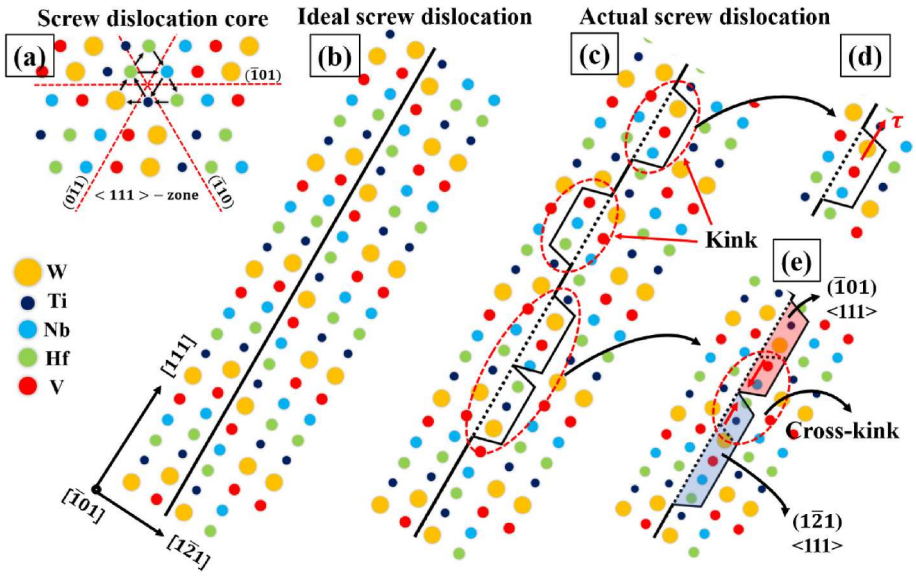

Fig. 14. Screw dislocation structure of the $Ti_{37}V_{15}Nb_{22}Hf_{23}W_3$ RHEA: (a) Screw dislocation in the 5-component random alloy (colors indicate species). Arrows indicate the characteristic three-fold symmetric compact core in pure BCC alloys. The dislocation can kink on any {110} plane of the <111>-zone. (b) A long and straight screw dislocation under ideal conditions. (c) The actual screw dislocation after kink is formed spontaneously due to composition fluctuation and thermal activation. (d) The slipping of a screw dislocation along the direction of the dislocation line under stress. (e) A kink formed when screw dislocations on different sliding planes meet. (For interpretation of the references to color in this figure legend, the reader is referred to the Web version of this article.)

Table 5
The lattice constant (a), shear modulus (G), Modulus of elasticity (E), individual atomic volume (V_n), and atomic misfit volume ($\Delta\overline{V}_n$) of the element and the studied alloy.

Element	Ti	V	Nb	Hf	W
a (pm)	327.6	303.9	330.1	355.9	315.8
G (GPa)	43.9	46.7	37.5	28.5	160.5
E (GPa)	116	128	105	78	411
V_n (Å^3)	17.58	14.03	17.98	22.54	15.75
$\Delta\overline{V}_n$ (Å^3)	−0.64	−4.19	−0.24	4.32	−2.48

Table 6
The Poisson's ratio (ν), zero-temperature shear yield stress (τ_{y0}), and the energy barrier for the thermal-activated at absolute zero (ΔE_{b0}) of the $Ti_{37}V_{15}Nb_{22}Hf_{23}W_3$ RHEA.

Alloy	ν	τ_{y0} (MPa)	ΔE_{b0} ($\times 10^{-19}$ J)
$Ti_{37}V_{15}Nb_{22}Hf_{23}W_3$	0.347	574.7	3.37

Table 7
Experimental and predicted tensile yield strengths of $Ti_{37}V_{15}Nb_{22}Hf_{23}W_3$ RHEA at different temperature.

Temperature (K)	σ_y (MPa)	
	Experimental	Predicted
293	977 ± 24	1080
373	893 ± 28	962
473	759 ± 13	855
673	697 ± 8	706
873	729 ± 20	555
973	648 ± 16	492
1073	575 ± 20	437
1223	186 ± 10	343

strengths of the $Ti_{37}V_{15}Nb_{22}Hf_{23}W_3$ RHEA at different temperatures. Fig. 15 compares the tensile yield strengths of theoretically predicted and experimental values. It can be observed that the tensile yield

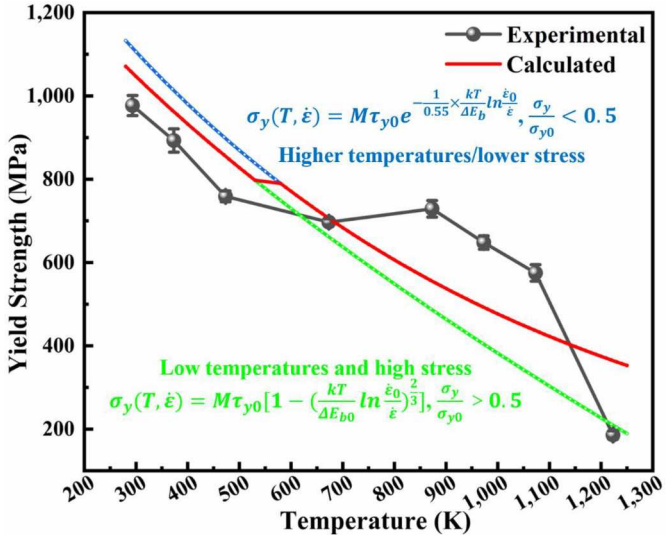

Fig. 15. Calculated yield strength as a function of the temperature for the $Ti_{37}V_{15}Nb_{22}Hf_{23}W_3$ RHEA by the edge-dislocation-strengthening model, compared with experimental data.

strength of the alloy, as predicted by the theory, decreases with the increasing temperatures. The predicted trend is in good agreement with the experimental results. However, it is found that the theoretical predicted value is higher than the actual value when the temperature is below 673 K (Fig. 15). It is due to that the edge dislocation strength model is used. According to the analysis in section 4.2, the dislocation involved in plastic deformation of the alloy is mainly screw dislocation at low and medium temperatures [25,76]. This means that less shear stress is required to start the screw dislocation. The edge dislocation strength model overestimates the yield strength of the alloy. At the same time, it is noted that the theoretical predicted value is lower than the experimental value at 873 K to 1,073 K (Fig. 15). This may be due to the following reasons: the $Ti_{37}V_{15}Nb_{22}Hf_{23}W_3$ RHEA smelted during the experiment contains impurities such as O, N and C. For example,

commercial raw materials Ti, V, Nb, Hf, and W inevitably contain impurities such as O, N and C with a mass fraction of about 1×10^{-16} [81]. These impurity elements tend to polarize around the dislocation and have a certain pinning effect on the dislocation, which may produce additional strengthening effects [82].

5. Conclusions

In summary, a novel $Ti_{37}V_{15}Nb_{22}Hf_{23}W_3$ RHEA has been developed, which presents excellent tensile mechanical properties over a wide temperature range of 298–1223 K. The conclusions are summarized as follows:

(1) The as-cast $Ti_{37}V_{15}Nb_{22}Hf_{23}W_3$ RHEA exhibits excellent resistance to high-temperature softening at elevated temperatures. An anomalous temperature-independent "high-temperature plateau" in the yield strength of the alloy was observed between 473 K and 873 K. During this tempearature range, the strength remained constant at 700–750 MPa. At the same time, when the temperature is 1073 K, the strength of the $Ti_{37}V_{15}Nb_{22}Hf_{23}W_3$ RHEA remains above 550 MPa, which already surpasses most superalloys.
(2) The causes of the 1,073 K brittle fracture are discussed and analyzed. In the time as short as 15 min, nano-sized precipitates were precipitated at the grain boundaries of the alloy. These precipitates cause stress concentration under loading, resulting in intergranular fracture.
(3) The yield strength of $Ti_{37}V_{15}Nb_{22}Hf_{23}W_3$ RHEA at different temperatures was predicted using the edge dislocation strength model. The predicted values are higher than the experimental values at low and medium temperatures, which is attributed to the large number of screw dislocations involved in the plastic deformation of the alloy. At higher temperatures, the predicted values are lower than the experimental values, probably due to the pinning effect of C, N, and O impurity elements on the edge dislocations, which produce additional strengthening.

Originality statement

We would like to declare that this is an original work that has not been published previously, and not under consideration for publication elsewhere, in whole or in part.

CRediT authorship contribution statement

Wenjun Huang: Writing – review & editing, Writing – original draft. **Xuejiao Wang:** Writing – review & editing, Methodology. **Junwei Qiao:** Writing – review & editing, Validation, Supervision, Conceptualization. **Xiaohui Shi:** Writing – review & editing, Methodology. **Peter K. Liaw:** Writing – review & editing, Supervision, Conceptualization. **Yucheng Wu:** Validation, Supervision, Methodology, Conceptualization.

Declaration of competing interest

This article is original. The article has been written by the stated authors that are all aware of its content and approve its submission. The article has not been published previously. The article is not under consideration for publication elsewhere. No conflict of interest exists, or if such conflict exists, the exact nature must be declared. If accepted, the article will not be published elsewhere in the same form, in any language, without the written consent of the publisher.

Data availability

Data will be made available on request.

Acknowledgments

J.W.Q. would like to acknowledge the financial support by the National Key Laboratory for Remanufacturing, Academy of Armored Forces Engineering (No. 61420050204), and the financial support of the State Key Lab of Advanced Metals and Materials (No. 2022-Z22). Y.C.W. would like to acknowledge financial supports from (1) the National Key Research and Development Program, China (Nos. 2014GB121000 and 2019YFE03120002), and (2) the National Natural Science Foundation (Nos. 514740830, 52020105014, and 51828101). X.J.W. would like to acknowledge the financial support of the Natural Science Foundation of Shanxi Province, China (No. 20210302124043). P. K. L. very much appreciate the support from (1) the National Science Foundation (DMR - 1611180, 1809640, and 2226508) and (2) the US Army Research Office (W911NF-13–1-0438 and W911NF-19–2-0049). X.H.S. would like to acknowledge the financial support of the Fundamental Research Program of Shanxi Province, China (No. 202203021211130).

References

[1] R. Feng, B. Feng, M.C. Gao, C. Zhang, J.C. Neuefeind, J.D. Poplawsky, Y. Ren, K. An, M. Widom, P.K. Liaw, Superior high-temperature strength in a supersaturated refractory high-entropy alloy, Adv. Mater. 33 (48) (2021) e2102401.
[2] B. Wei, Y. Lin, Z. Huang, L. Huang, K. Zhou, L. Zhang, L. Zhang, A novel Re-free Ni-based single-crystal superalloy with enhanced creep resistance and microstructure stability, Acta Mater. 240 (2022) 118336.
[3] A. Bhattacharya, Y.-F. Shen, M. Hefferan Christopher, F. Li Shiu, J. Lind, M. Suter Robert, E. Krill Carl, S. Rohrer Gregory, Grain boundary velocity and curvature are not correlated in Ni polycrystals, Science 374 (6564) (2021) 189–193.
[4] J.H. Perepezko, The hotter the engine, the better, Science 326 (5956) (2009) 1068–1069.
[5] O.N. Senkov, D.B. Miracle, K.J. Chaput, J.-P. Couzinie, Development and exploration of refractory high entropy alloys—a review, J. Mater. Res. 33 (19) (2018) 3092–3128.
[6] B. Wang, Q. Wang, N. Lu, X. Liang, B. Shen, Enhanced high-temperature strength of HfNbTaTiZrV refractory high-entropy alloy via Al2O3 reinforcement, J. Mater. Sci. Technol. 123 (2022) 191–200.
[7] W. Xia, X. Zhao, L. Yue, Z. Zhang, A review of composition evolution in Ni-based single crystal superalloys, J. Mater. Sci. Technol. 44 (2020) 76–95.
[8] C. Liu, J. Cui, Z. Cheng, B. Zhang, S. Zhang, J. Ding, R. Yu, E. Ma, Direct observation of oxygen atoms taking tetrahedral interstitial sites in medium-entropy body-centered-cubic solutions, Adv. Mater. (2023) e2209941.
[9] E.P. George, W.A. Curtin, C.C. Tasan, High entropy alloys: a focused review of mechanical properties and deformation mechanisms, Acta Mater. 188 (2020) 435–474.
[10] Z. Li, S. Zhao, R.O. Ritchie, M.A. Meyers, Mechanical properties of high-entropy alloys with emphasis on face-centered cubic alloys, Prog. Mater. Sci. 102 (2019) 296–345.
[11] E.P. George, D. Raabe, R.O. Ritchie, High-entropy alloys, Nat. Rev. Mater. 4 (8) (2019) 515–534.
[12] J.W. Yeh, S.K. Chen, S.J. Lin, J.Y. Gan, T.S. Chin, T.T. Shun, C.H. Tsau, S.Y. Chang, Nanostructured high-entropy alloys with multiple principal elements: novel alloy design concepts and outcomes, Adv. Eng. Mater. 6 (5) (2004) 299–303.
[13] B. Cantor, I.T.H. Chang, P. Knight, A.J.B. Vincent, Microstructural development in equiatomic multicomponent alloys, Mater. Sci. Eng., A 375–377 (2004) 213–218.
[14] B. Yin, W.A. Curtin, Origin of high strength in the CoCrFeNiPd high-entropy alloy, Mater. Res. Lett. 8 (6) (2020) 209–215.
[15] S. Liu, W. Kai, J. Hou, Y. Zhao, Q. Li, C.-h. Yang, T. Yang, J.-j. Kai, Oxidation behaviors and mechanical properties of L12-strengthened high-entropy alloys at 700 °C, Corrosion Sci. 206 (2022) 110499.
[16] Z. An, S. Mao, T. Yang, Y. Liu, Y. Chen, X. Yang, S. Liu, X. Wang, Q. Deng, Z. Zhang, X. Han, Simultaneously enhanced oxidation resistance and mechanical properties in a novel lightweight Ti2VZrNb0.5Al0.5 high-entropy alloy, Sci. China Mater. 65 (10) (2022) 2842–2849.
[17] J.L. Yuan, Z. Wang, X. Jin, P.D. Han, J.W. Qiao, L12-strengthened heterostructure high-entropy alloys with ultra-high strength over a wide temperature range, Mater. Sci. Eng., A 853 (2022) 143712.
[18] W. Li, D. Xie, D. Li, Y. Zhang, Y. Gao, P.K. Liaw, Mechanical behavior of high-entropy alloys, Prog. Mater. Sci. 118 (2021) 100777.
[19] D.B. Miracle, O.N. Senkov, A critical review of high entropy alloys and related concepts, Acta Mater. 122 (2017) 448–511.
[20] O.N. Senkov, G.B. Wilks, J.M. Scott, D.B. Miracle, Mechanical properties of Nb25Mo25Ta25W25 and V20Nb20Mo20Ta20W20 refractory high entropy alloys, Intermetallics 19 (5) (2011) 698–706.
[21] O.N. Senkov, J.M. Scott, S.V. Senkova, D.B. Miracle, C.F. Woodward, Microstructure and room temperature properties of a high-entropy TaNbHfZrTi alloy, J. Alloys Compd. 509 (20) (2011) 6043–6048.

[22] B.G. Butler, J.D. Paramore, J.P. Ligda, C. Ren, Z.Z. Fang, S.C. Middlemas, K. J. Hemker, Mechanisms of deformation and ductility in tungsten – a review, Int. J. Refract. Metals Hard Mater. 75 (2018) 248–261.
[23] G. Dirras, J. Gubicza, A. Heczel, L. Lilensten, J.P. Couzinié, L. Perrière, I. Guillot, A. Hocini, Microstructural investigation of plastically deformed Ti20Zr20Hf20Nb20Ta20 high entropy alloy by X-ray diffraction and transmission electron microscopy, Mater. Char. 108 (2015) 1–7.
[24] J.P. Couzinié, L. Lilensten, Y. Champion, G. Dirras, L. Perrière, I. Guillot, On the room temperature deformation mechanisms of a TiZrHfNbTa refractory high-entropy alloy, Mater. Sci. Eng., A 645 (2015) 255–263.
[25] F. Maresca, W.A. Curtin, Mechanistic origin of high strength in refractory BCC high entropy alloys up to 1900K, Acta Mater. 182 (2020) 235–249.
[26] C. Lee, F. Maresca, R. Feng, Y. Chou, T. Ungar, M. Widom, K. An, J.D. Poplawsky, Y.-C. Chou, P.K. Liaw, W.A. Curtin, Strength can be controlled by edge dislocations in refractory high-entropy alloys, Nat. Commun. 12 (1) (2021) 5474.
[27] W. Huang, J. Hou, X. Wang, J. Qiao, Y. Wu, Excellent room-temperature tensile ductility in as-cast Ti37V15Nb22Hf23W3 refractory high entropy alloys, Intermetallics 151 (2022) 107735.
[28] W. Huang, S. Yin, X. Wang, R. Guo, Y. Wu, J. Qiao, Grain growth and Hall–Petch relationship in Ti37V15Nb22Hf23W3 refractory high-entropy alloys, J. Mater. Res. 38 (6) (2023) 1719–1729.
[29] C. Zhang, H. Wang, X. Wang, Y.T. Tang, Q. Yu, C. Zhu, M. Xu, S. Zhao, R. Kou, X. Wang, B.E. MacDonald, R.C. Reed, K.S. Vecchio, P. Cao, T.J. Rupert, E. J. Lavernia, Strong and ductile refractory high-entropy alloys with super formability, Acta Mater. 245 (2023).
[30] L.H. Mills, M.G. Emigh, C.H. Frey, N.R. Philips, S.P. Murray, J. Shin, D.S. Gianola, T.M. Pollock, Temperature-dependent tensile behavior of the HfNbTaTiZr multi-principal element alloy, Acta Mater. 245 (2023) 118618.
[31] Q. Liu, L. Fang, Z. Xiong, J. Yang, Y. Tan, Y. Liu, Y. Zhang, Q. Tan, C. Hao, L. Cao, J. Li, Z. Gao, The response of dislocations, low angle grain boundaries and high angle grain boundaries at high strain rates, Mater. Sci. Eng., A 822 (2021) 141704.
[32] L. Zhang, Y. Gu, Y. Xiang, Energy of low angle grain boundaries based on continuum dislocation structure, Acta Mater. 126 (2017) 11–24.
[33] W.D. Callister, D.G. Rethwisch, Materials Science and Engineering, Wiley, United States of America, 2012.
[34] L.T.W. Smith, Y. Su, S. Xu, A. Hunter, I.J. Beyerlein, The effect of local chemical ordering on Frank-Read source activation in a refractory multi-principal element alloy, Int. J. Plast. 134 (2020) 102850.
[35] A.G. Quarrell, The hardness of metals, Nature 170 (4333) (1952) 818.
[36] S. He, X. Zhou, D. Mordehai, J. Marian, Thermal super-jogs control the high-temperature strength plateau in Nb-Mo-Ta-W alloys, Acta Mater. 244 (2023) 118539.
[37] H. Zhang, Y. Zhao, J. Cai, S. Ji, J. Geng, X. Sun, D. Li, High-strength NbMoTaX refractory high-entropy alloy with low stacking fault energy eutectic phase via laser additive manufacturing, Mater. Des. 201 (2021) 109462.
[38] R.R. Eleti, N. Stepanov, N. Yurchenko, S. Zherebtsov, F. Maresca, Cross-kink unpinning controls the medium- to high-temperature strength of body-centered cubic NbTiZr medium-entropy alloy, Scripta Mater. 209 (2022) 114367.
[39] A. Ghafarollahi, F. Maresca, W.A. Curtin, Solute/screw dislocation interaction energy parameter for strengthening in bcc dilute to high entropy alloys, Model. Simulat. Mater. Sci. Eng. 27 (8) (2019) 085011.
[40] F. Maresca, W.A. Curtin, Theory of screw dislocation strengthening in random BCC alloys from dilute to “High-Entropy” alloys, Acta Mater. 182 (2020) 144–162.
[41] A. Ghafarollahi, W.A. Curtin, Screw-controlled strength of BCC non-dilute and high-entropy alloys, Acta Mater. 226 (2022) 117617.
[42] X.F. Xie, Z.M. Xie, R. Liu, Q.F. Fang, C.S. Liu, W.-Z. Han, X. Wu, Hierarchical microstructures enabled excellent low-temperature strength-ductility synergy in bulk pure tungsten, Acta Mater. 228 (2022) 117765.
[43] A.H. Cottrell, Theory of dislocations, Prog. Met. Phys. 4 (1953) 205–264.
[44] A.S. Argon, Strengthening Mechanisms in Crystal Plasticity, Oxford University Press, 2007.
[45] A. Pineau, Preface to overviews of failure of metals, Acta Mater. 107 (2016) 423.
[46] X. Yan, P.K. Liaw, Y. Zhang, Ultrastrong and ductile BCC high-entropy alloys with low-density via dislocation regulation and nanoprecipitates, J. Mater. Sci. Technol. 110 (2022) 109–116.
[47] Y. Jia, G. Wang, S. Wu, Y. Mu, Y. Yi, Y. Jia, P.K. Liaw, T. Zhang, C.-T. Liu, A lightweight refractory complex concentrated alloy with high strength and uniform ductility, Appl. Mater. Today 27 (2022) 101429.
[48] O.N. Senkov, J.M. Scott, S.V. Senkova, F. Meisenkothen, D.B. Miracle, C. F. Woodward, Microstructure and elevated temperature properties of a refractory TaNbHfZrTi alloy, J. Mater. Sci. 47 (9) (2012) 4062–4074.
[49] O.N. Senkov, S. Gorsse, D.B. Miracle, High temperature strength of refractory complex concentrated alloys, Acta Mater. 175 (2019) 394–405.
[50] D. Caillard, J. Martin, Thermally Activated Mechanisms in Crystal Plasticity, 2003.
[51] W. Jiang, P. Xu, Y. Li, H. Wang, Z. Cai, J. Li, Y. Liang, Y. Liang, Effect of a gradient structure on the mechanical performance of Inconel 718 Ni-based superalloy at elevated temperatures, J. Mater. Res. Technol. 23 (2023) 2031–2042.
[52] A. De Bartolomeis, S.T. Newman, I.S. Jawahir, D. Biermann, A. Shokrani, Future research directions in the machining of Inconel 718, J. Mater. Process. Technol. 297 (2021) 117260.
[53] X. Yan, Y. Zhang, Y. Zou, Near-superplastic behavior of a body-centered cubic Zr50Ti35Nb15 multi-principal element alloy via dynamic recrystallization, Scripta Mater. 227 (2023) 115308.
[54] M.J. Sohrabi, H. Mirzadeh, S. Sadeghpour, R. Mahmudi, Grain size dependent mechanical behavior and TRIP effect in a metastable austenitic stainless steel, Int. J. Plast. 160 (2023) 103502.
[55] L. Li, Z. Zhang, P. Zhang, Z. Zhang, A review on the fatigue cracking of twin boundaries: crystallographic orientation and stacking fault energy, Prog. Mater. Sci. 131 (2023) 101011.
[56] A. Kanchi, K.V. Rajulapati, B.S. Rao, D. Sivaprahasam, R.C. Gundakaram, Influence of thermomechanical processing on microstructure and mechanical properties of moNbTaW refractory high-entropy alloy, J. Mater. Eng. Perform. 31 (10) (2022) 7964–7972.
[57] J.R. Rice, Dislocation nucleation from a crack tip: an analysis based on the Peierls concept, J. Mech. Phys. Solid. 40 (2) (1992) 239–271.
[58] V.I. Trefilov, Y. Milman, I.V. Gridneva, Characteristic temperature of deformation of crystalline materials, Cryst. Res. Technol. 19 (1984) 413–421.
[59] D. Rupp, R. Mönig, P. Gruber, S.M. Weygand, Fracture toughness and microstructural characterization of polycrystalline rolled tungsten, Int. J. Refract. Metals Hard Mater. 28 (6) (2010) 669–673.
[60] C. Yin, D. Terentyev, T. Zhang, S. Nogami, S. Antusch, C.-C. Chang, R.H. Petrov, T. Pardoen, Ductile to brittle transition temperature of advanced tungsten alloys for nuclear fusion applications deduced by miniaturized three-point bending tests, Int. J. Refract. Metals Hard Mater. 95 (2021) 105464.
[61] C. Ren, Z.Z. Fang, L. Xu, J.P. Ligda, J.D. Paramore, B.G. Butler, An investigation of the microstructure and ductility of annealed cold-rolled tungsten, Acta Mater. 162 (2019) 202–213.
[62] Y. Cheng, M. Mrovec, P. Gumbsch, Atomistic simulations of interactions between the 1/2⟨111⟩ edge dislocation and symmetric tilt grain boundaries in tungsten, Phil. Mag. 88 (4) (2008) 547–560.
[63] E. Smiti, P. Jouffrey, A. Kobylanski, The influence of carbon and oxygen in the grain boundary on the brittle-ductile transition temperature of tungsten Bi-crystals, Scripta Metall. 18 (7) (1984) 673–676.
[64] W.A.T. Clark, R.H. Wagoner, Z.Y. Shen, T.C. Lee, I.M. Robertson, H.K. Birnbaum, On the criteria for slip transmission across interfaces in polycrystals, Scripta Metall. Mater. 26 (2) (1992) 203–206.
[65] Z. Shen, R.H. Wagoner, W.A.T. Clark, Dislocation and grain boundary interactions in metals, Acta Metall. 36 (12) (1988) 3231–3242.
[66] A. Misra, R. Gibala, Room-temperature deformation behavior of directionally solidified multiphase Ni-Fe-Al alloys, Metall. Mater. Trans. 28 (3) (1997) 795–807.
[67] R.D. Noebe, A. Misra, R. Gibala, Plastic flow and fracture of B2 NiAl-based intermetallic alloys containing a ductile second phase, ISIJ Int. 31 (1991) 1172–1185.
[68] J. Reiser, J. Hoffmann, U. Jäntsch, M. Klimenkov, S. Bonk, C. Bonnekoh, M. Rieth, A. Hoffmann, T. Mrotzek, Ductilisation of tungsten (W): on the shift of the brittle-to-ductile transition (BDT) to lower temperatures through cold rolling, Int. J. Refract. Metals Hard Mater. 54 (2016) 351–369.
[69] J.R. Rice, R. Thomson, Ductile versus brittle behaviour of crystals, Phil. Mag.: J. Theor. Exp. Appl. Phys. 29 (1) (1974) 73–97.
[70] Y. Lu, Y.H. Zhang, E. Ma, W.Z. Han, Relative mobility of screw versus edge dislocations controls the ductile-to-brittle transition in metals, Proc. Natl. Acad. Sci. USA 118 (37) (2021) e2110596118.
[71] J.X. Hou, S.F. Liu, B.X. Cao, J.H. Luan, Y.L. Zhao, Z. Chen, Q. Zhang, X.J. Liu, C. T. Liu, J.J. Kai, T. Yang, Designing nanoparticles-strengthened high-entropy alloys with simultaneously enhanced strength-ductility synergy at both room and elevated temperatures, Acta Mater. 238 (2022) 118216.
[72] J.W. Christian, Some surprising features of the plastic deformation of body-centered cubic metals and alloys, Metall. Trans. A 14 (7) (1983) 1237–1256.
[73] M. Tanaka, E. Tarleton, S.G. Roberts, The brittle–ductile transition in single-crystal iron, Acta Mater. 56 (18) (2008) 5123–5129.
[74] K.S. Chan, A grain boundary fracture model for predicting dynamic embrittlement and oxidation-induced cracking in superalloys, Metall. Mater. Trans. 46 (6) (2015) 2491–2505.
[75] C.T. Liu, C.L. White, Dynamic embrittlement of boron-doped Ni3Al alloys at 600°C, Acta Metall. 35 (3) (1987) 643–649.
[76] F. Wang, G.H. Balbus, S. Xu, Y. Su, J. Shin, P.F. Rottmann, K.E. Knipling, J.-C. Stinville, L.H. Mills, O.N. Senkov, I.J. Beyerlein, T.M. Pollock, D.S. Gianola, Multiplicity of dislocation pathways in a refractory multiprincipal element alloy, Science 370 (6512) (2020) 95–101.
[77] G. Monnet, D. Terentyev, Structure and mobility of the 12<111>{112} edge dislocation in BCC iron studied by molecular dynamics, Acta Mater. 57 (5) (2009) 1416–1426.
[78] H. Cho, C.A. Bronkhorst, H.M. Mourad, J.R. Mayeur, D.J. Luscher, Anomalous plasticity of body-centered-cubic crystals with non-Schmid effect, Int. J. Solid Struct. 139–140 (2018) 138–149.
[79] Y. Lu, Y.-H. Zhang, E. Ma, W.-Z. Han, Relative mobility of screw versus edge dislocations controls the ductile-to-brittle transition in metals, Proc. Natl. Acad. Sci. USA 118 (37) (2021).
[80] C. Varvenne, A. Luque, W.A. Curtin, Theory of strengthening in fcc high entropy alloys, Acta Mater. 118 (2016) 164–176.
[81] X. Zhang, J. Tian, M. Xue, F. Jiang, S. Li, B. Zhang, J. Ding, X. Li, E. Ma, X. Ding, J. Sun, Ta-W refractory alloys with high strength at 2000°C, Acta Metall. Sin. 58 (2022) 1253–1260.
[82] Z. Wang, H. Wu, Y. Wu, H. Huang, X. Zhu, Y. Zhang, H. Zhu, X. Yuan, Q. Chen, S. Wang, X. Liu, H. Wang, S. Jiang, M.J. Kim, Z. Lu, Solving oxygen embrittlement of refractory high-entropy alloy via grain boundary engineering, Mater. Today 54 (2022) 83–89.